EXPERIMENTAL STUDY OF MULTI-STAGE ACID JETTING IN CARBONATE ROCKS

A Thesis

by

EMMANUEL PALON BELOSTRINO

Submitted to the Office of Graduate and Professional Studies of
Texas A&M University
in partial fulfillment of the requirements for the degree of

MASTER OF SCIENCE

Chair of Committee,	Ding Zhu
Committee Members,	A. Daniel Hill
	Yuefeng Sun
Head of Department,	A. Daniel Hill

December 2016

Major Subject: Petroleum Engineering

ABSTRACT

High-velocity jetting of acid in carbonate formations as a stimulation technique is an emerging technology currently being studied for applications in long horizontal wells. One way to achieve this is by using limited entry liners and nozzles designed to control the placement of acid along the lateral. Previous field-testing has successfully shown desirable acid distribution along an extended reach well with formation heterogeneities. To support the modeling of this stimulation process, seminal laboratory experiments were previously conducted by jetting 15% (by weight) hydrochloric acid (HCl) through limestone cores. Preceding experimental studies showed the formation of bulb-shaped cavities at the jetted surface, and the propagation of wormholes from these cavities. These initial studies revealed that the formation of cavities and wormholes are greatly affected by jetting velocity, interstitial velocity, and permeability.

However, the mechanism of both the cavity formation and wormhole propagation in the core samples still remains unclear. This study aims to better understand these processes by performing acid jetting laboratory experiments with a modified procedure. The new experiments divide acid jetting in multiples stages to produce data snapshots and computed tomography (CT) scan images throughout the cavity and wormhole development in a rock sample. 15% HCl was jetted at constant pressures, with velocities between 107 ft/s and 200 ft/s through six Indiana limestone cores, with permeability measurements ranging from 2.4 mD to 6.9 mD, and porosities around 14%. For each core, multiple jetting stages were conducted until breakthrough stage was reached. Initial

interstitial velocity was set at 0.5 cm/min for all cases, which increased to an average of around 1 cm/min around breakthrough point. After each jetting stage, CT scan images and other physical data of the core were obtained before placing it back in the injection setup for the next jetting stage. Injection times for each stage ranged from 1.3 minutes to 4.1 minutes, and each core underwent jetting for three to six stages.

CT scan data of the cores were processed and 3D-rendered, producing high-definition multi-angle snapshots of the rock dissolution progression through time. The results clearly demonstrate that cavities and wormholes develop concurrently during acid jetting. It was observed that rock samples with higher permeabilities form larger cavities, and similarly would create larger cavities at higher injection rates.

These results are of significant use in future experimental and modeling studies of acid jetting, which are needed for upscaling to well stimulation design in the field.

DEDICATION

I dedicate this work to my family, friends, mentors, colleagues, motivators, and all the hardworking graduate students in the world.

ACKNOWLEDGEMENTS

Firstly, I would like to thank the chair of my committee, Dr. Ding Zhu, for guiding me throughout the process of completing my masters degree and for giving me the opportunity to work on this project. Being part of her research group has truly been an enjoyable learning experience, both inside and outside the walls of the petroleum engineering building. I would also like to thank Dr. A. Daniel Hill and Dr. Yuefeng Sun for their insightful guidance and contributions as members of my graduate committee.

Moreover, I would like to thank Vanessa Ndonhong and Christopher Holland for paving the way in exploring experimental acid jetting. Their previous works have been instrumental in pursuing this study. Vanessa has been especially helpful in guiding me throughout the process of learning the subject matter. In addition, I would like to thank our hardworking undergraduate research assistants, William Tarpley and Spencer Omsberg, for helping me in performing the experiments and processing the data. I would also like to express my appreciation to Taylor Frick and Dmitry Ridner for their help and for being excellent graduate student trainees. The future of this research project is bright under their steering.

Many thanks should also be given to the faculty, staff, students, and all other people at the Harold Vance Department of Petroleum Engineering at Texas A&M University for the wonderful graduate school experience.

I would like to express my gratitude to ExxonMobil Upstream Research Company, for their financial and technical support throughout the study. Dr. Richard Beckman and Dr. Renzo Angeles have both been instrumental in pursuing this study.

Finally, I would like to thank my family, friends, classmates, and colleagues for their love, support, and encouragement from the beginning to the end.

CONTRIBUTORS AND FUNDING SOURCES

Contributors

This study was supervised by a thesis committee consisting of Dr. Ding Zhu and Dr. A. Daniel Hill of the Harold Vance Department of Petroleum Engineering and Dr. Yuefeng Sun of the Department of Geology and Geophysics.

The laboratory experiments were performed with the assistance of Vanessa Ndonhong and William Tarpley of the Harold Vance Department of Petroleum Engineering.

All other work conducted for the thesis was completed by the student independently.

Funding Sources

This work was supported by a research assistantship from Texas A&M Engineering Experiment Station and industry partner ExxonMobil Upstream Research Company.

The contents of the study are solely the responsibility of the author and do not necessarily represent the official views of the ExxonMobil.

NOMENCLATURE

A	Cross-sectional area of the core
A_{nozzle}	Cross-sectional area of the nozzle
CT	Computed Tomography
D_{core}	Diameter of the core
DICOM	Digital Imaging and Communications in Medicine
D_{nozzle}	Inner diameter of the nozzle
HCl	Hydrochloric acid
k	Permeability
KOH	Potassium hydroxide
L	Length of the core
m_{dry}	Dry mass
m_{sat}	Saturated mass
n	Number of stages
q	Flow rate through the core
$q_{effluent}$	Effluent flow rate
q_{max}	Maximum pump flow rate
q_{pump}	Pump flow rate
V_{bulk}	Bulk volume
v_i	Interstitial velocity
v_{jet}	Jetting velocity

V_{pore}	Pore volume
$\Delta L_{wormhole}$	Wormhole length increment
ΔP	Pressure differential
Δt_{stage}	Jetting time for each stage
ΔV_{cavity}	Cavity volume increment
$\Delta W_{effluent}$	Weight difference after each stage
μ	Viscosity
ρ_w	Density of water
ϕ	Porosity

TABLE OF CONTENTS

Page

ABSTRACT ii

DEDICATION iv

ACKNOWLEDGEMENTS v

CONTRIBUTORS AND FUNDING SOURCES vii

Contributors vii
Funding Sources vii

NOMENCLATURE viii

TABLE OF CONTENTS x

LIST OF FIGURES xii

LIST OF TABLES xv

1. INTRODUCTION 1

1.1 Background on Acid Stimulation for Long Horizontal Wells 1
1.2 Acid Jetting Using Limited Entry Liners 2
1.3 Jetting Applications in the Oilfield 3
1.4 Experimental Acid Jetting 4
1.5 Research Objectives 9

2. METHODOLOGY 11

2.1 Rock Sample Preparation and Property Measurement 11
2.1.1 Core Saturation with Water 11
2.1.2 Permeability Measurement 13
2.1.3 Porosity Calculation 16
2.1.4 Desired Pressure Differential Calculation 17
2.2 Acid Jetting in Multiple Stages 18
2.2.1 Acid Jetting Experimental Setup 18
2.2.2 Acid Jetting Experimental Procedure 24
2.3 CT Image Processing 33

3. RESULTS AND DISCUSSION 40

3.1 Average Interstitial Velocity Calculation....41
3.2 Acid Concentration Analysis....46
3.3 CT Image Processing Results....47
3.4 Wormhole Growth and Growth Rates....52
3.5 Cavity Growth and Growth Rates....57

4. CONCLUSIONS, RECOMMENDATIONS & FUTURE WORK....62

REFERENCES....64

APPENDIX....66

LIST OF FIGURES

Page

Figure 1.1. Fluid flow in a limited entry liner completion with packers (Sau et al., 2014a). 3

Figure 1.2. Cavity and wormholes formed from acid jetting (Holland, 2014)..... 5

Figure 1.3. Development of dissolution structures as interstitial velocity is increased (Ndonhong et al., 2016). 7

Figure 1.4. Computation fluid dynamics simulation of a turbulent jet impinging on a cavity (Beckham et al., 2015). 9

Figure 2.1. Indiana limestone rock samples used in the study. 12

Figure 2.2. Water saturation setup (core container and vacuum pump)..... 13

Figure 2.3. Permeability testing apparatus. 14

Figure 2.4. Schematic diagram of the permeability testing apparatus (Grabski, 2012). .. 15

Figure 2.5. LabView program for permeability measurement. 16

Figure 2.6. Schematic diagram of the acid jetting setup (Holland, 2014). 18

Figure 2.7. Chem/Meter pulse pump. 19

Figure 2.8. Acid jetting core holder parts (Holland, 2014). 20

Figure 2.9 Inlet cap cross section (Holland, 2014). 21

Figure 2.10. Acid jetting LabView program (Holland, 2014)..... 23

Figure 2.11. Acid jetting setup with all the connections attached. 27

Figure 2.12. Emerald timestamp application for iOS. 29

Figure 2.13. Toshiba Aquilion CT scan machine. 32

Figure 2.14. OsiriX database screen. 34

Figure 2.15. Four sets of CT images viewed using Horos. 35

Figure 2.16. Pre-processing of CT images. 36

Figure 2.17. 3D volume rendering of the dissolution structures. 37

Figure 2.17. Wormhole length calculation. 38

Figure 2.18. Cavity volume calculation through cross-sectional area integration. 39

Figure 3.1. Average interstitial velocity per stage. 44

Figure 3.2. Average interstitial velocity per stage (breakthrough stage considered as outlier) 45

Figure 3.3. Acid concentration as jetting progressed. 47

Figure 3.4. IC01 (107 ft/s, higher *k*) acid jetting dissolution through time. 49

Figure 3.5. IC02 (107 ft/s, lower *k*) acid jetting dissolution through time. 49

Figure 3.6. IC03 (150 ft/s, higher *k*) acid jetting dissolution through time. 50

Figure 3.7. IC05 (150 ft/s, lower *k*) acid jetting dissolution through time. 50

Figure 3.8. IC04 (200 ft/s, higher *k*) acid jetting dissolution through time. 51

Figure 3.9. IC06 (200 ft/s, lower *k*) acid jetting dissolution through time. 51

Figure 3.10. Wormhole length versus cumulative jetting time. 52

Figure 3.11. Wormhole growth rate per stage versus cumulative jetting time. 53

Figure 3.12. Average wormhole growth rate calculation through linear regression (v_{jet} = 107 ft/s) 55

Figure 3.13. Average wormhole growth rate calculation through linear regression (v_{jet} = 150 ft/s) 56

Figure 3.14. Average wormhole growth rate calculation through linear regression (v_{jet} = 200 ft/s) 56

Figure 3.15. Cavity volume versus cumulative jetting time. 58

Figure 3.16. Cavity volume growth rate per stage versus cumulative jetting time. 58

Figure 3.17. Average cavity growth rate calculation through linear regression (v_{jet} = 150 ft/s). 59

Figure 3.18. Average cavity growth rate calculation through linear regression (v_{jet} = 150 ft/s). 60

Figure 3.19. Average cavity growth rate calculation through linear regression (v_{jet} = 200 ft/s). 60

Figure A.1. Post-jetting core images showing cavities (top view). 66

Figure A.2. Post-jetting core images showing wormholes (bottom view). 67

Figure A.3. Excel file for results processing. 68

Figure A.4. IC01 (v_{jet} = 107 ft/s, k = 4.01 mD) multi-stage acid jetting results. 69

Figure A.5. IC02 (v_{jet} = 107 ft/s, k = 2.43 mD) acid jetting results. 70

Figure A.6. IC03 (v_{jet} = 150 ft/s, k = 6.87 mD) acid jetting results. 71

Figure A.7. IC05 (v_{jet} = 150 ft/s, k = 2.38 mD) acid jetting results. 72

Figure A.8. IC04 (v_{jet} = 200 ft/s, k = 5.30 mD) acid jetting results. 73

Figure A.9. IC06 (v_{jet} = 200 ft/s, k = 3.53 mD) acid jetting results. 74

LIST OF TABLES

Page

Table 3.1. Core preparation results summary. 41

Table 3.2. Experimental parameters and interstitial velocity. 43

Table 3.3. Average wormhole growth rates for each rock sample, calculated through linear regression. 55

Table 3.4. Average cavity growth rates for each rock sample, calculated through linear regression. 59

Table A.1. IC01 (v_{jet} = 107 ft/s, k = 4.01 mD) CT image processing results. 75

Table A.2. IC02 (v_{jet} = 107 ft/s, k = 2.43 mD) CT image processing results. 75

Table A.3. IC03 (v_{jet} = 150 ft/s, k = 6.87 mD) CT image processing results. 76

Table A.4. IC05 (v_{jet} = 150 ft/s, k = 2.38 mD) CT image processing results. 76

Table A.5. IC04 (v_{jet} = 200 ft/s, k = 5.30 mD) CT image processing results. 77

Table A.6. IC06 (v_{jet} = 200 ft/s, k = 3.53 mD) CT image processing results. 77

1. INTRODUCTION

1.1 Background on Acid Stimulation for Long Horizontal Wells

The advent of new technologies in drilling engineering and well construction has made it possible to construct extended reach horizontal wells with very long completions. As wells are drilled longer, greater reservoir contact is achieved. While this is generally a desirable case, difficulties may arise, however, due to the heterogeneity in the formation along the lateral. Heterogeneity may be manifested by variations in lithology, permeability, pressure, or temperature within the reservoir.

In carbonate reservoirs, heterogeneity is especially common due to their complex rock fabric. This brings challenges when carbonate formations undergo acid stimulation. In an ideal scenario, acid is distributed uniformly throughout the areas of reservoir contact. The acid then dissolves the rock and creates wormholes that bypass formation damage and lower the formation skin factor, which consequently improve well productivity. However in the presence of heterogeneity, acid may preferentially flow through the zones of lower flow resistance (i.e., zones with higher permeability and/or lower skin factor), leaving the higher flow resistance zones with low or no acid flow at all. Controlling the flow of acid is therefore necessary for such cases. This can be achieved by mechanical (e.g. use of coiled tubing, ball sealers, or drill pipe placement) or chemical (e.g. using gelled acids, viscoelastic surfactants, or emulsified acid) means of diversion (Kalfayan and Martin, 2009). One method to place acid that has recently been developed is the use of limited entry liners and small widely spaced nozzles placed throughout the lateral completion.

1.2 Acid Jetting Using Limited Entry Liners

The use of limited entry liners for acid stimulation of extended reach wells can be more advantageous than traditional methods (stimulation using coiled tubing, drill pipe, or diverters) as it addresses challenges such as reach limitations, operational complexities, acid exposure times, and high costs (Beckham et al., 2015).

Figure 1.1 shows a fluid flow model through a limited entry liner completion with isolation packers (Sau et al., 2014a). Uniform distribution of acid is achieved using limited entry liners in open hole completions by engineering the local pressure drop across each liner by designing it with regard to the adjacent formation properties. Using sparsely placed small nozzles along the extent of the completion, the desired pressure drops can be controlled. Lowering the number of nozzles along the zones of lower flow resistance allows greater volumes of acid to be placed along high flow resistance zones. This requires zonal isolation packers to prevent short-circuiting of acid flow into the annulus in zones with high resistance to flow (Sau et al., 2014b).

A recent field test on an extended reach horizontal well using limited entry liners and nozzles demonstrated the successful distribution of bullheaded acid along its 11,200-ft completion (Shuchart et al., 2014).

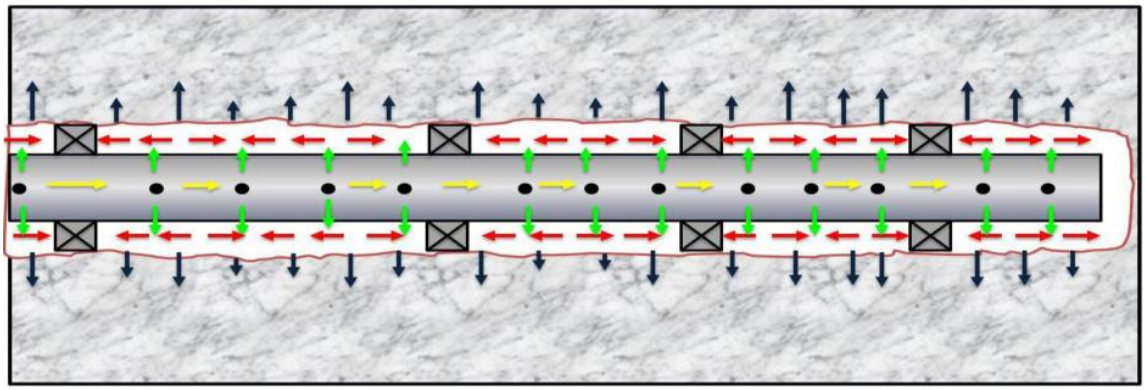

Figure 1.1. Fluid flow in a limited entry liner completion with packers (Sau et al., 2014a).

1.3 Jetting Applications in the Oilfield

The use of jetting in the oilfield is not a new concept, and its use in various applications has been previously explored. Johnson et al. (1998) developed a system of jetting abrasive slurries to clean scales inside the well tubing. A rotating nozzle head with a speed-control system and high-pressure coiled tubing were designed for this purpose. Surjaatmadja et al. (1994) pioneered the hydrajetting technology as a completion technique to perforate the wellbore and as a means to initiate fractures using a jet of high-pressure water.

Well stimulation techniques similar to acid jetting using limited entry liners and nozzles have been successfully used in the past. One directly comparable method is the Controlled Acid Jet completion and stimulation technique (Hansen and Nederveen, 2002). This technology makes use of high-velocity acid released from pre-drilled holes along a non-cemented liner. It has been proven successful in placing acid and stimulating long horizontal wells in carbonate formations (Denney, 2002; Carpenter, 2013).

One notable difference between the Controlled Acid Jet technique and limited entry liner acid jetting is that the latter makes use of isolation packers to segment the stimulated zones along the lateral prior to acid bullheading, while the former does not. In addition, the limited entry liners are stationary while the Controlled Acid Jet liners are non-cemented.

1.4 Experimental Acid Jetting

When acid is injected through nozzles, it flows at a very high velocity. Matrix acidizing and acid jetting are similar in that both stimulation techniques involve injection of acid below the formation fracture pressure. The key difference with acid jetting is that it combines both the effects of chemical reaction and mechanical action when creating wormholes. In addition to the chemical reaction between the acid and the carbonate rock, injection of fluid through high-differential pressure nozzles creates a highly turbulent flow and localized pressure points where the jet impinges. Fundamental understanding of the acid jetting process is therefore necessary in order to better design the diversion and stimulation jobs in the field. Experimental studies perform a key function in achieving this.

The seminal acid jetting experiments performed by Holland (2014) using Indiana limestone cores (4 inches in diameter and 16 inches in length) revealed the presence of bulb-shaped cavities and dominant wormholes attached to them (Figure 1.2). Wormhole breakthrough only occurred at runs with higher interstitial velocities. It was also observed that cores that underwent jetting at higher jetting velocities form deeper cavities, but no

conclusions on the cavity growth and wormhole propagation were drawn. In addition, the original study concluded that acid jetting could not be directly compared with matrix acidizing in terms of determining optimum conditions due to the presence of the cavities and the variable flux (interstitial velocity) through the core.

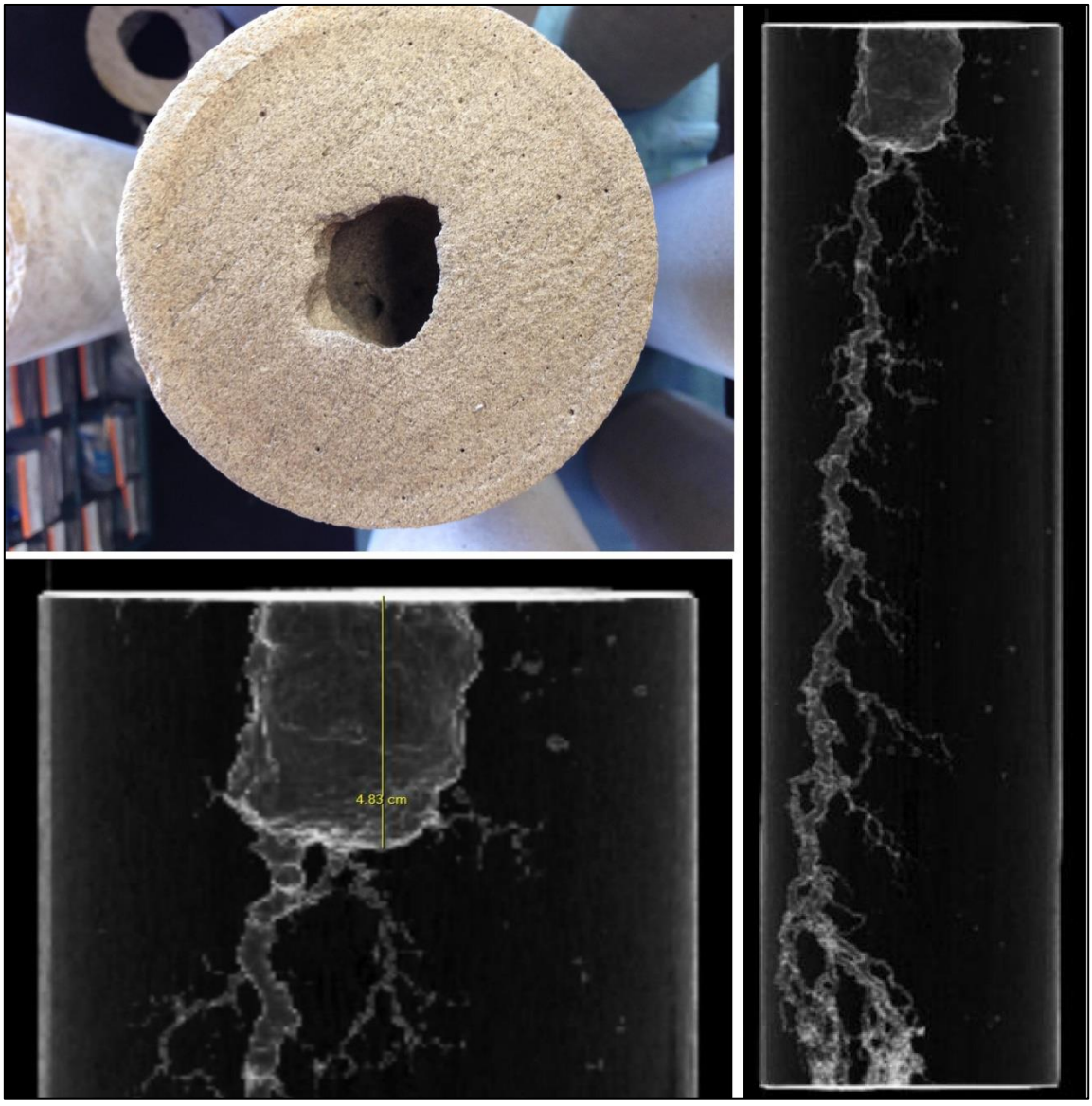

Figure 1.2. Cavity and wormholes formed from acid jetting (Holland, 2014).

The succeeding experimental study then focused on the effects of fundamental rock properties and laboratory parameters on the dissolution structures created by acid jetting (Ndonhong, 2014; Ndonhong et al., 2016). The study suggested that acid jetting is similar to matrix acidizing in terms of the manner of the dissolution structure formation with respect to the average interstitial velocity through the core. That is, it was proposed that for a constant jetting velocity, an optimum interstitial velocity occurs which creates dominant wormholes – below which cavity formation is more dominant, and above which, wormhole propagation is more dominant that heavy branching occurs (Figure 1.3). The two competing dissolution phenomena in acid jetting are both important, and experimental results showed that jetting velocity is the dominant parameter for cavity formation, while interstitial velocity dominates wormhole propagation. Therefore, a balance between jetting velocity and interstitial velocity is necessary to develop both cavities and wormholes in acid jetting.

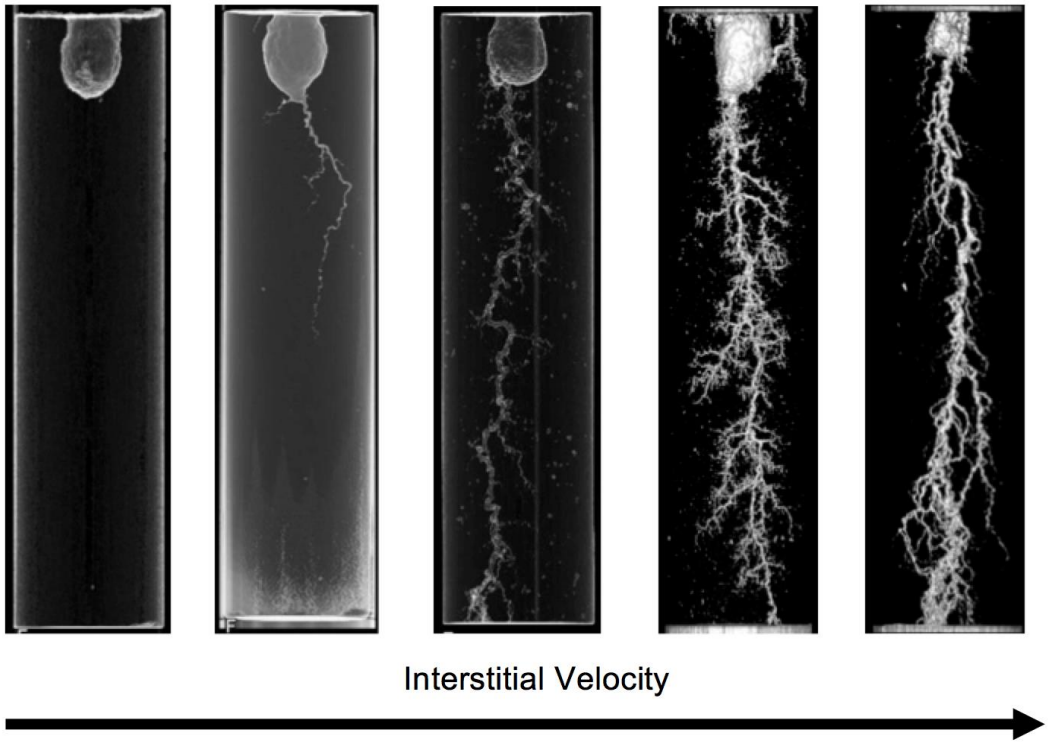

Figure 1.3. Development of dissolution structures as interstitial velocity is increased (Ndonhong et al., 2016).

Ndonhong, et al. (2016) also investigated the effects of temperature and rock type on acid jetting. Initial high-temperature experiments showed that increasing the temperature inhibits wormhole development, and promotes cavity formation. Winterset limestone rocks, which have lower permeability, higher porosity and a more heterogeneous rock fabric, show different dissolution patterns than those of the more permeable, less porous and more homogeneous Indiana limestone samples.

These earlier studies have therefore established that the critical parameters that affect cavity and wormhole propagation during acid jetting are jetting velocity, interstitial velocity, permeability, temperature, pore structure, and mineralogy. Among these

parameters, jetting velocity and interstitial velocity are the ones that can be straightforwardly controlled when performing laboratory experiments. Moreover, these two parameters have the most impact on the manner dissolution structures are formed during acid jetting.

Initial work on the modeling of experimental acid jetting has already initiated. Using computational fluid dynamics simulation, Beckham et al. (2015) modeled cavity formation to initiate from a substantial increase in local acid flux created by the localized surface pressure spike around the central point where the turbulent jet impinges on the rock. Two mechanisms of carbonate dissolution are then proposed to be active after cavity formation – traditional matrix dissolution and surface dissolution. Matrix dissolution is enhanced by the pressure increase created by the jet's kinetic energy, while surface dissolution inside the cavity is accelerated by the turbulent flow along the walls, resulting to the enlargement of the cavity as jetting progresses (Figure 1.4).

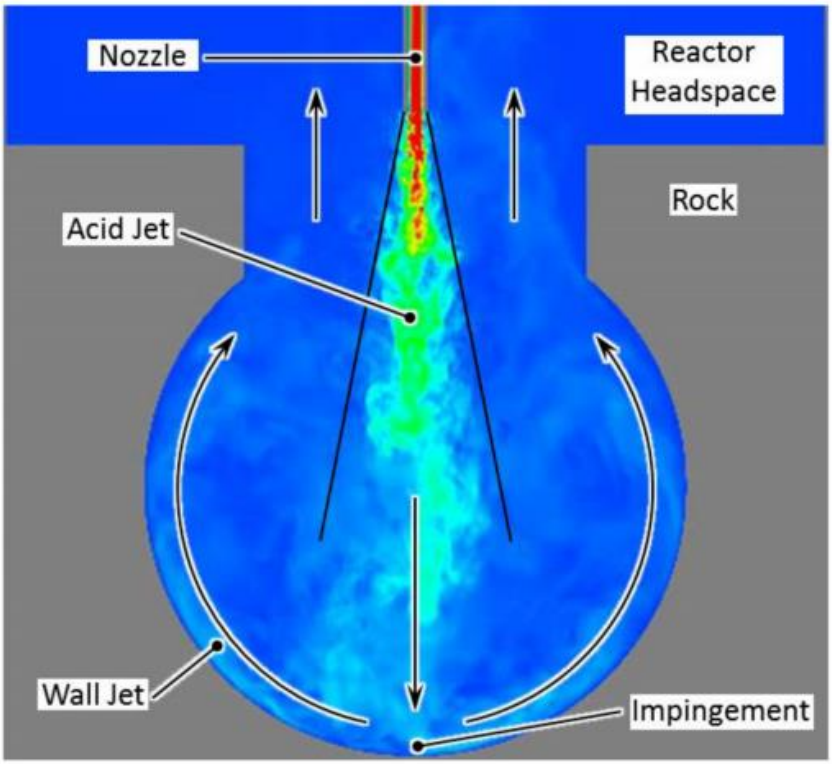

Figure 1.4. Computation fluid dynamics simulation of a turbulent jet impinging on a cavity (Beckham et al., 2015).

Despite these fundamental results, the mechanism of both cavity formation and wormhole propagation during acid jetting still remains unclear. It is necessary to understand these processes better in order to successfully model the process of experimental acid jetting.

1.5 Research Objectives

The goal of this study is to further lay the groundwork in understanding the dissolution phenomena that occur during acid jetting through a modified laboratory procedure that allows data collection throughout the jetting process. It aims to learn more

about the competition occurring during the development of dissolution structures. It seeks to answer the question of whether the cavity or the wormhole develops first before the other, or if they grow simultaneously. Moreover, better understanding of cavity and wormhole growth rates can be provided by the experiment results.

An ideal process is to constantly record computer tomography (CT) images of core samples from the beginning to the end of an experiment, which can then be processed to produce complete 4-dimensional analyses. Unfortunately, such approach is practically impossible due to the constraints of the required equipment.

This study develops a new acid jetting experimental procedure that uses multiple stage injections to capture snapshots of cavity and wormhole growth. It appropriated the same set up and procedures use in previous laboratory jetting experiments (Holland, 2014; Ndonhong, 2014) using Indiana limestone cores, conducted in multiple stages for each rock sample. Post-processing and 3-dimensional (3D) rendering of the CT images provide clear snapshots of the rock dissolution progression. The primary parameters studied are permeability, jetting velocity, breakthrough times, wormhole length and growth rates, cavity size and growth rates, and average interstitial velocities.

2. METHODOLOGY

The methodology used in the study is divided into three parts: (1) preparation of rock samples and property calculation, (2) acid jetting in multiple stages, and (3) CT image processing.

The cores are prepared prior to jetting by saturating them with water. The permeability, porosity, and the desired pressure differential are subsequently calculated for each rock sample. Acid jetting is then performed in multiple stages. Each stage starts with the pre-flush injection of water to the core, followed by the jetting of acid for a specified time, and ends with the post-flush water injection. Analysis of CT data involves the CT scanning of the rocks after each jetting stage, and the processing of these images to produce the results.

2.1 Rock Sample Preparation and Property Measurement

2.1.1 Core Saturation with Water

The Indiana limestone core samples used in this study are from Kocurek Industries. Each core is 4 inches in diameter and 16 inches in length. Each of the six cores is labeled with a corresponding identification number (IC01, IC02, IC03, IC04, IC05, and IC06) using a permanent marker (Figure 2.1). In addition, a straight line marking is drawn along the length of the core to ensure consistent positioning during jetting and CT scanning. The dry weight of each core is then recorded.

Figure 2.1. Indiana limestone rock samples used in the study.

Prior to permeability testing and acid jetting, the cores are fully water-saturated. Each core is placed in a cylindrical plastic container filled close to the brim with water. The container is then capped tightly with a lid, which is connected to the intake of a vacuum pump (Leybold Trivac Model D2A) by a tube (Figure 2.2). The vacuum pump facilitates the saturation process by continuously suctioning air from the closed rock-water system in the container. Application of vacuum grease and continual monitoring are necessary to ensure that the vacuum pressure is at least 70 kPa. Each core is saturated for at least eight hours.

Figure 2.2. Water saturation setup (core container and vacuum pump).

2.1.2 Permeability Measurement

Once the cores are fully water-saturated, permeability measurement follows. The permeability test setup consists of the core holder, constant-flow syringe pump, water accumulator, pressure transducer, hydraulic oil pump, tubing, and a computer with a LabView program for permeability measurement installed (Figure 2.3). Grabski's (2012) work provides a detailed description of the permeability-testing setup, which is a subset

of a matrix acidizing core flooding apparatus. Figure 2.4 shows a schematic diagram of the setup.

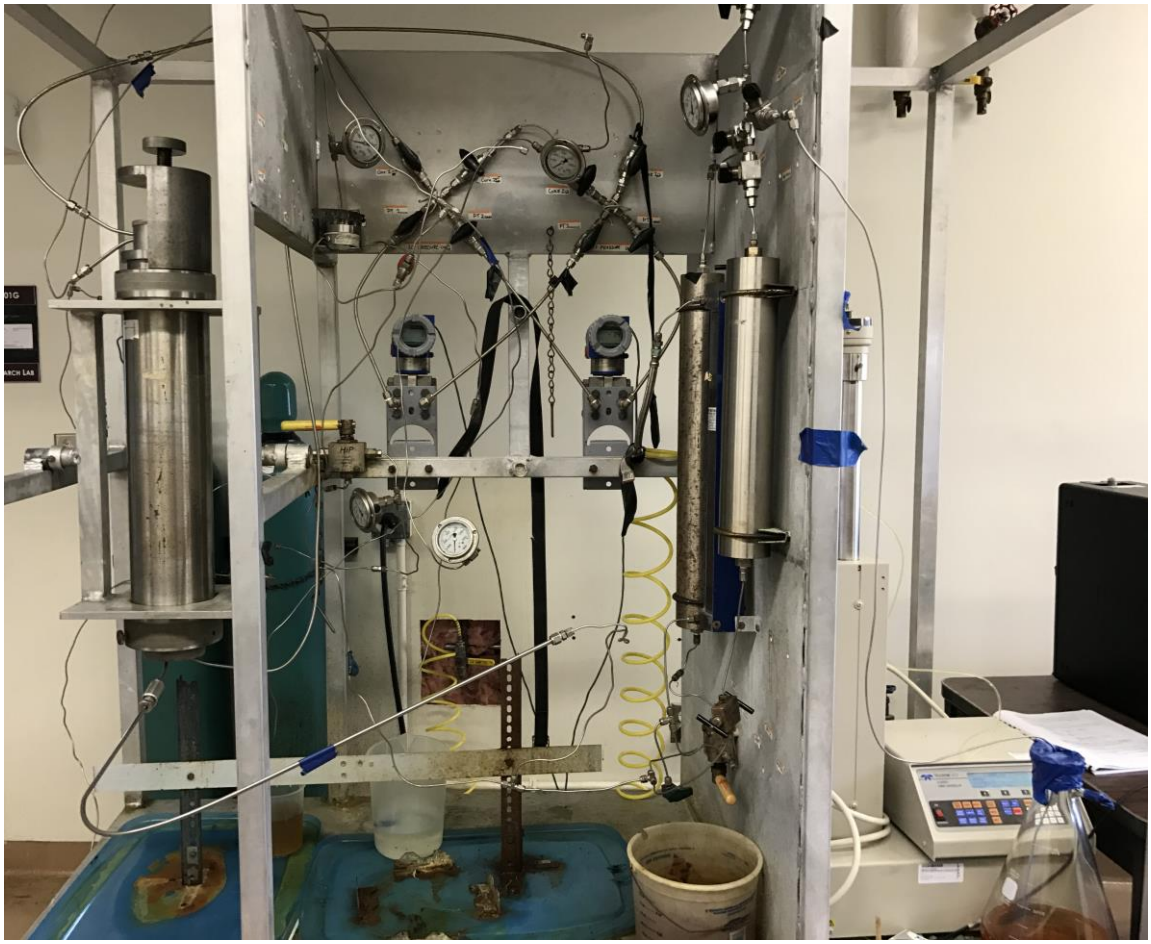

Figure 2.3. Permeability testing apparatus.

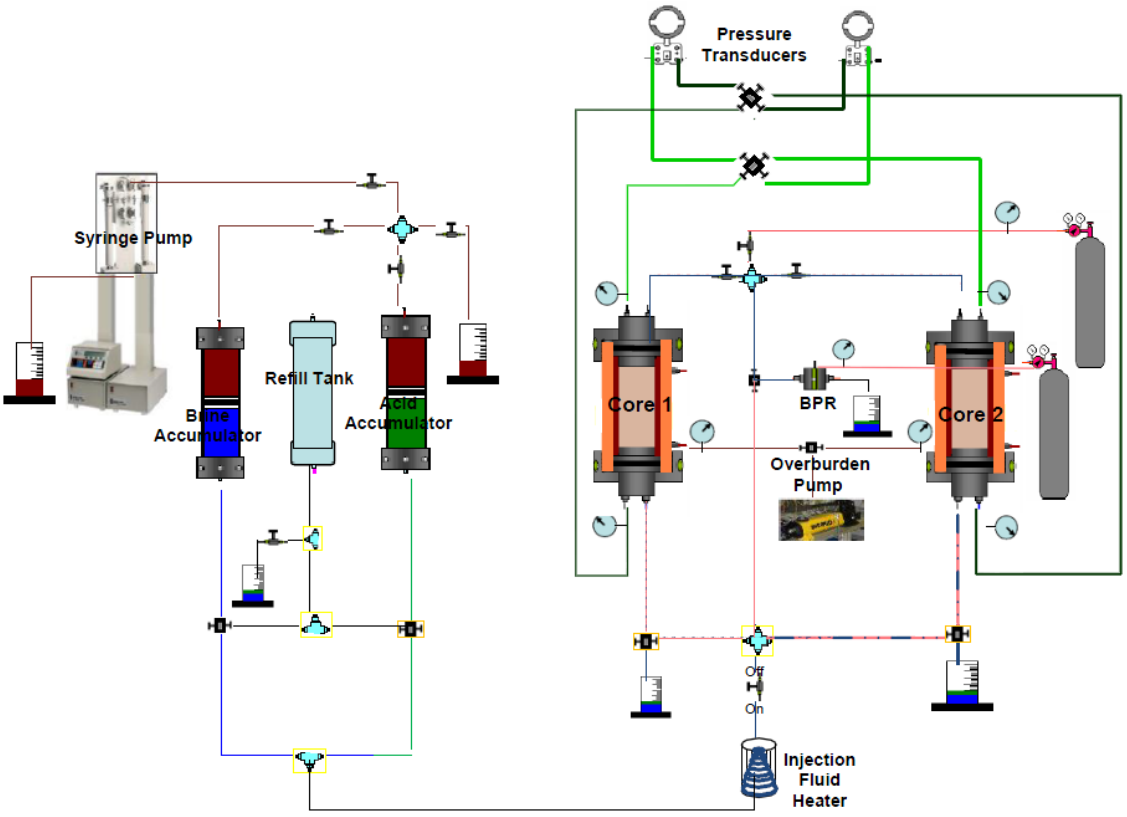

Figure 2.4. Schematic diagram of the permeability testing apparatus (Grabski, 2012).

Water is injected to the core at a constant rate and the difference in pressure between the core inlet and outlet is recorded and monitored through the LabView program (Figure 2.5). Once at a stable, constant pressure differential, the permeability (k) of each core is calculated through Darcy's law, as shown by Equation 2.1.

$$k = \frac{96.13qL\mu}{\Delta PA} \tag{2.1}$$

In the equation, the resulting permeability is in mD, and the flowrate (q) in cm^3/min, core length (L) in inches, viscosity (μ) in cp, pressure differential (ΔP) in psi, and core cross-sectional (A) in square inches. The pressure difference is regarded as stable after 15

minutes of constant values measured. A step-by-step procedure of the operation of the equipment, use of the LabView program, and permeability calculation is described by Holland (2014).

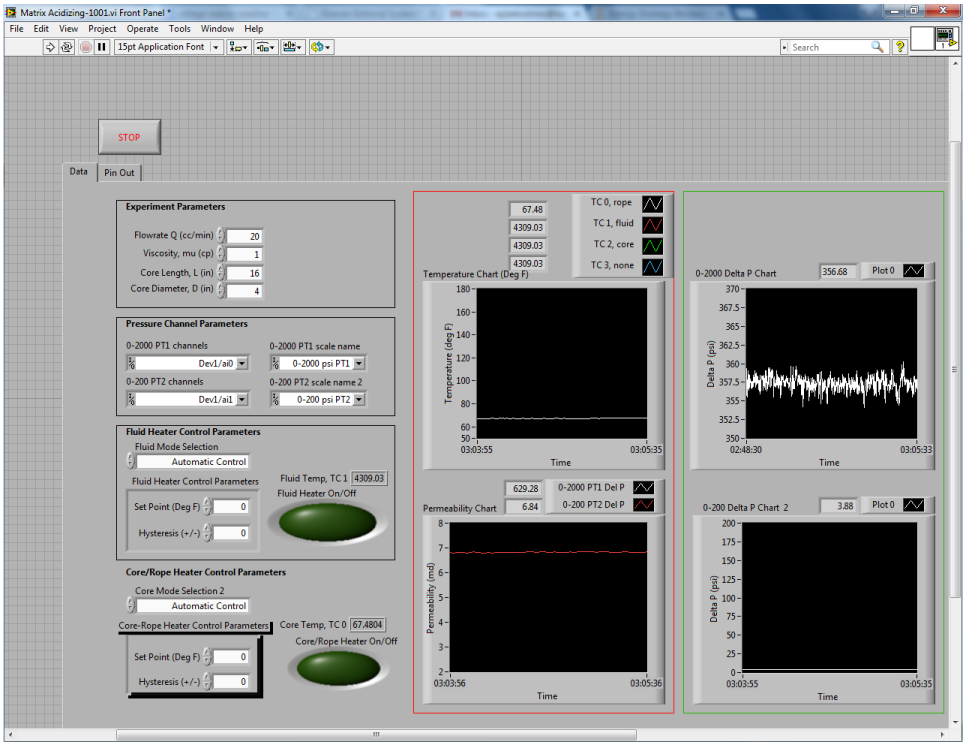

Figure 2.5. LabView program for permeability measurement.

2.1.3 Porosity Calculation

The saturated weight of each core is then recorded after permeability measurement. The dry and saturated weights of the six cores are used to calculate the corresponding porosities. Equation 2.2 shows the porosity (ϕ) calculation by obtaining the ratio of the pore volume (V_{pore}) and bulk volume (V_{bulk}) of the core. In the equation, core diameter

(D_{core}) and core length (L) are converted to centimeters, saturated weight (m_{sat}) and dry weight (m_{dry}) of the core is in grams, and the density of water (ρ_{water}) is 1 g/cm^3.

$$\phi = \frac{V_{pore}}{V_{bulk}} = \frac{\frac{m_{sat} - m_{dry}}{\rho_{water}}}{\frac{\pi}{4} D_{core}^2 L} \tag{2.2}$$

2.1.4 Desired Pressure Differential Calculation

The previous experiments (Holland, 2014; Ndonhong, 2014) have determined that interstitial velocity, jetting velocity, and permeability are among the most important parameters that control acid jetting. In order to limit the unknowns and to effectively compare the results of the study, interstitial velocity is controlled in the experiment. Previous matrix acidizing experiments (Dong et al., 2012) using 4-inch diameter, 8-inch length Indiana limestone cores with permeability values between 4 and 7 mD showed that the optimum interstitial velocity for 15% HCl at room temperature is about 1 cm/min. This optimum value is used as the desired average interstitial velocity right after breakthrough for all the six cases. In order to achieve this desired value, an initial interstitial velocity of around 0.5 cm/min is set. This value is based on previous observations that the average interstitial velocity increased to about twice the initial value after breakthrough.

The desired pressure differential values for each is then calculated using Equation 2.3 and setting v_i to 0.5 cm/min. The units are the same as those in Equation 2.1.

$$\Delta P = \frac{qL\mu}{96.13kA}; \text{where } q = v_i \phi A \tag{2.3}$$

2.2 Acid Jetting in Multiple Stages

2.2.1 Acid Jetting Experimental Setup

The primary components of the experimental acid jetting setup are a pulse pump, a core holder, two nitrogen tanks that supply pressure to upstream and downstream backpressure regulators, chemical containers, and a data acquisition system (Figure 2.6).

A pulse pump (Chem/Meter 802) provides the mechanical work for the fluid flow in the experiment (Figure 2.7). It has a maximum flow rate of 16.3 gallons per hour, and a maximum operating pressure of 2,200 psi. The fluid intake of the pump is initially connected to a water tank prior to acid jetting. A valve allows the switching of the fluid intake from the water tank to the acid container when acid jetting is to begin. The pump discharge is connected to the nozzle line of the inlet holder, which is later described in the succeeding paragraphs.

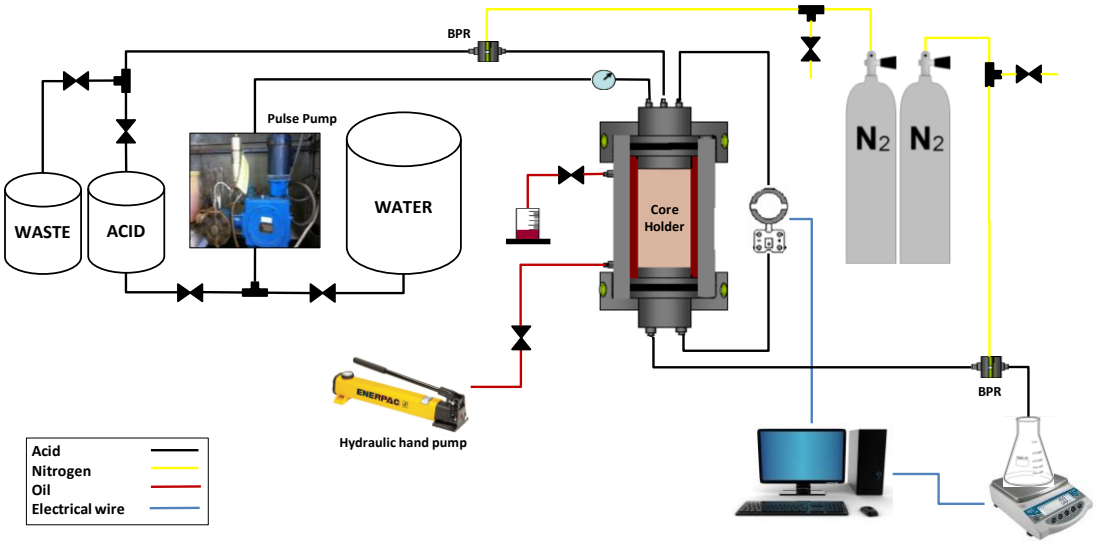

Figure 2.6. Schematic diagram of the acid jetting setup (Holland, 2014).

Figure 2.7. Chem/Meter pulse pump.

A cylindrical Hastelloy core holder (Figure 2.8A) contains the carbonate cores. Metal caps close off both ends of the core holder (Figure 2.8C and 2.8E). The top of the cylinder has the inlet holder that secures the inlet cap of the core. The inlet cap has three lines connected to it – the inlet line, the return line, and the pressure transducer line (Figures 2.8B and 2.9).

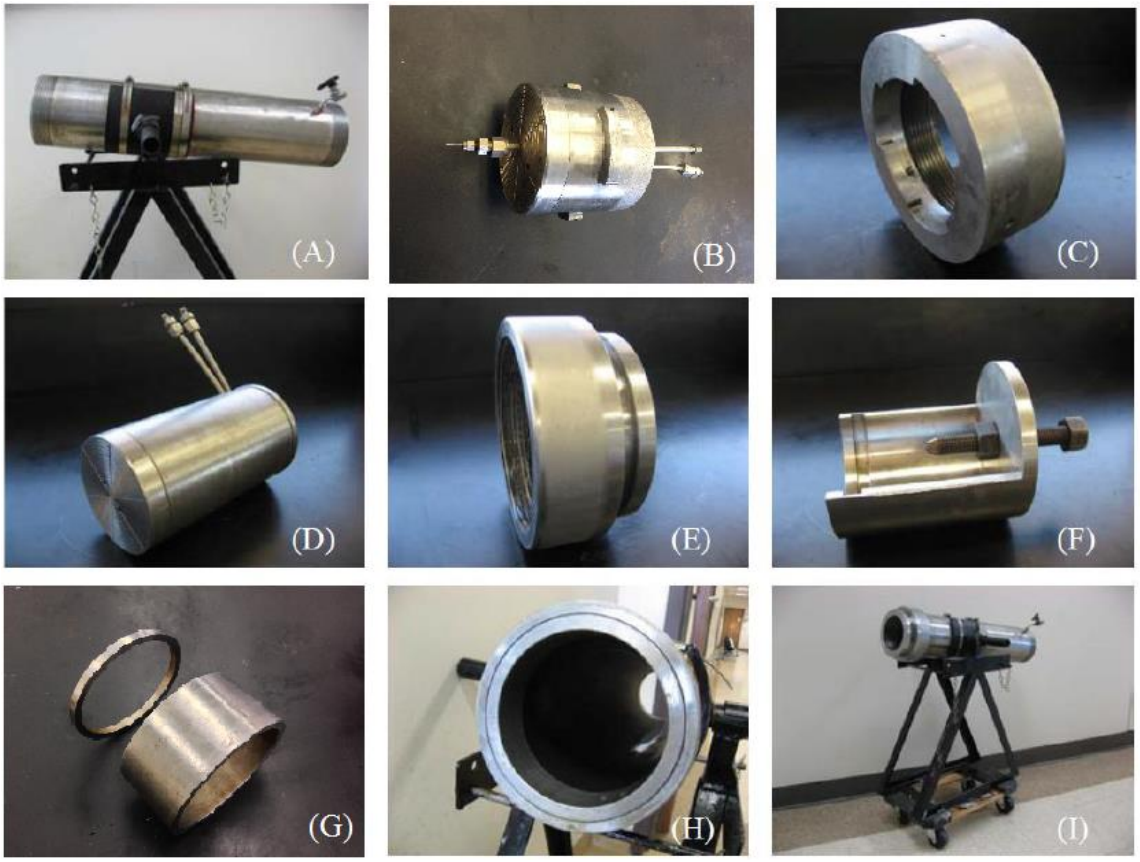

Figure 2.8. Acid jetting core holder parts (Holland, 2014).

Figure 2.9 shows the cross-section of the inlet cap where the nozzle is attached. A 1/4-inch diameter inlet line goes through the inlet cap, and on the other side that faced the core is the 1/16-inch outer diameter nozzle. Two spacer rings (Figure 2.8G) are placed in between the inlet cap and the core surface – one with a length of 2 inches and one with a length of 0.25 inch, for a total spacer length of 2.25 inches. Similar to the previous acid jetting experimental studies, a stand-off distance from the nozzle outlet to the core of surface of 0.09 inch is used, which corresponds to four times the inner diameter (0.0225 inch) of the nozzle. By obtaining the difference between the total spacer length and stand-off distance, the length of the nozzle tubing is determined, and it is equal to 2.16 inches.

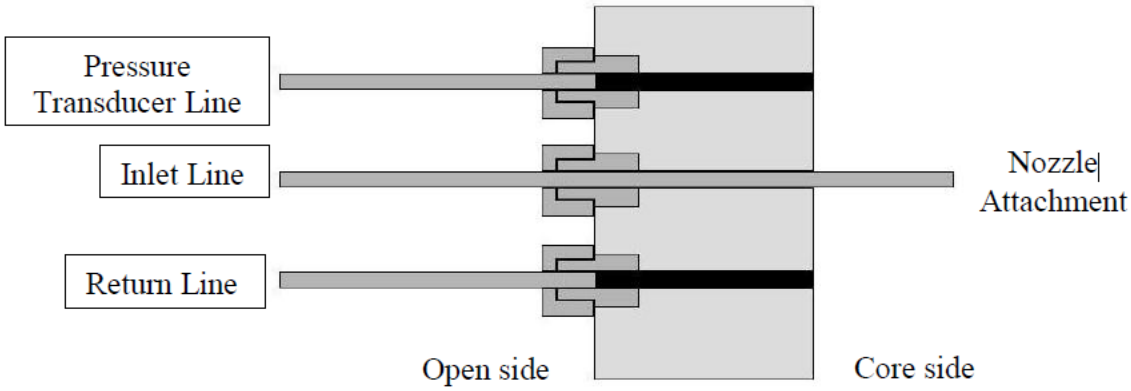

Figure 2.9 Inlet cap cross section (Holland, 2014).

Unlike the inlet line, the return line and the pressure transducer line of the inlet holder do not go all the way through the other side of the inlet cap, and are only connected to the outer open side (Figure 2.9). The 1/8-inch outer diameter pressure transducer line is connected to a pressure transducer (Foxboro model IDP10-A26E21F-M1) that measures the pressure differential across the core. The 1/4-inch diameter return line is connected to the upstream backpressure regulator (Mity-Mite S-91W), which controls the inlet pressure in the core holder. The backpressure regulator is connected to a nitrogen gas tank that sets the desired inlet pressure. To maintain the desired inlet pressure, a recycle line serves as the outlet line, which flows back to the acid tank (when jetting acid) or the waste tank (when jetting water).

Inside the core holder body, a custom-made Viton 70-75 fluoroelastomer sleeve (Phoenix Instruments) holds the core sample tightly in place. Hydraulic oil (Pro-Select AW-32) is pumped into the space between the sleeve and the inside wall of the core holder to provide confining pressure that prevents fluids from flowing along the sidewall of the core. An inlet and an outlet valve allow the inflow and outflow of hydraulic oil through

the annulus between the sleeve and core holder inner wall. A hydraulic hand pump (Enerpac P392) controls the amount of oil entering the inlet valve. Connected to the hydraulic oil outlet valve is a 1/8-inch outlet line that flows to a beaker, which collects the effluent hydraulic oil.

On the other side of the core holder is the outlet cap (Figure 2.8D) that secures the lower end of the core in place. This piece is set in place by an outlet lock (Figure 2.8F). Connected to it are two lines – the outlet line and the downstream backpressure line. The outlet line is attached to the pressure transducer. The downstream backpressure line is attached to the downstream backpressure regulator (Equilibar EB1HP1-SS316), which, similar to the upstream one, is connected to another nitrogen gas tank set at 1,000 psi throughout the experiments. Whenever the outlet pressure exceeds this 1,000 psi value, an effluent line releases fluid to an Erlenmeyer flask placed on top of a digital weighing scale (Ohaus SP4001). The change in the effluent weight corresponds to the flow rate through the core, which is thereby used to calculate interstitial velocity.

The pressure transducer and the digital weighing scale are both connected to a National Instruments processing board and a computer. A LabView program for acid jetting data acquisition is installed on the computer, which displays and records pressure differential and effluent weight values (Figure 2.10).

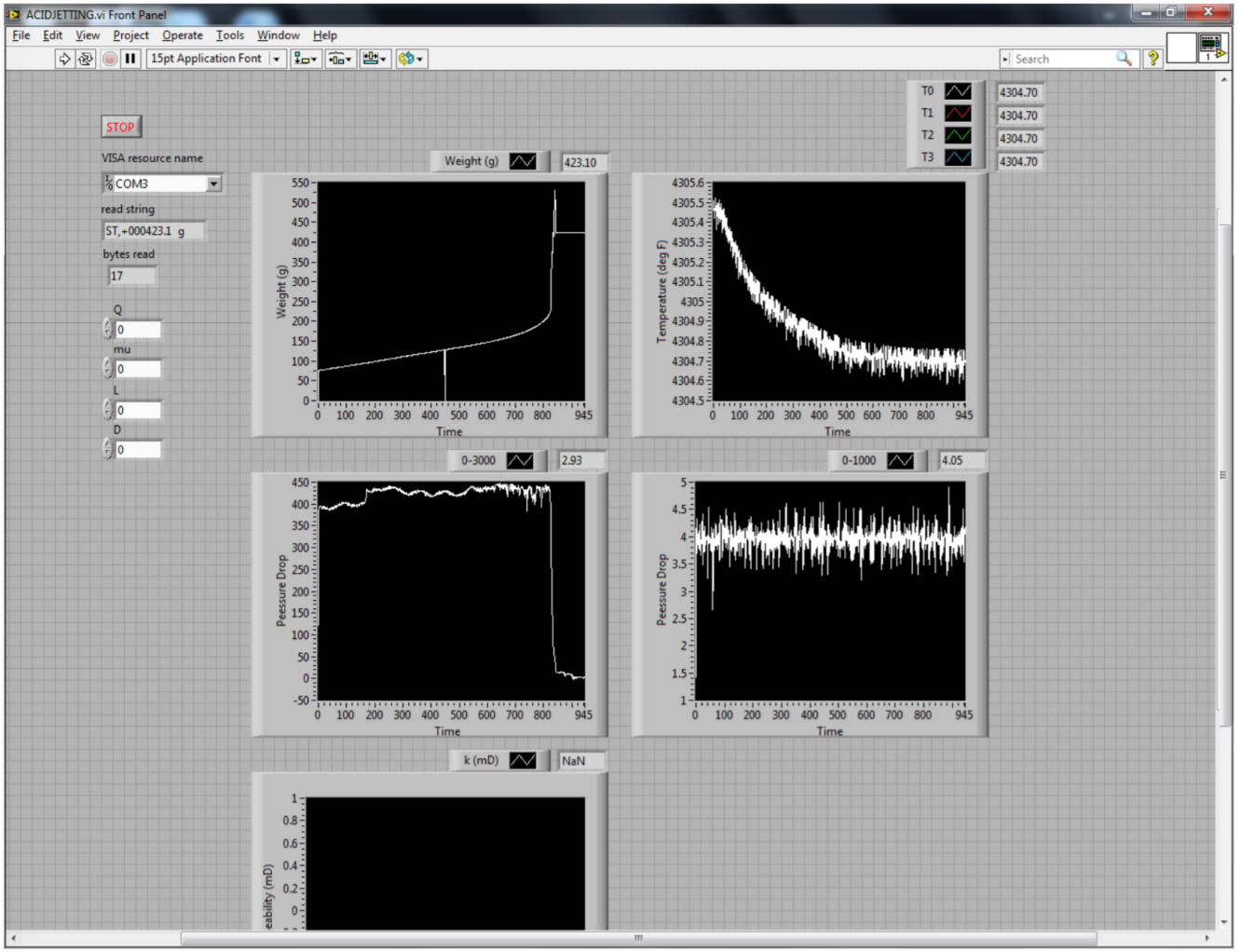

Figure 2.10. Acid jetting LabView program (Holland, 2014).

All of the pieces of tubing and connections are made of 316 stainless steel from Swagelok.

A more detailed description of the pieces of equipment used in the study can be found in Holland's (2014) seminal experimental study.

2.2.2 Acid Jetting Experimental Procedure

Five liters of 15% by weight HCl needs to be prepared by mixing 1,865 mL of 36.46% by weight HCl (Macron Chemical Company) with 3,135 mL water. It is important to note that acid should be poured into water, and not water into acid, to prevent violent physical reactions. Moreover, handling of acid should be performed under a fume hood, while wearing a gas mask or a face shield, and an extra layer of rubber gloves to ensure safety and protection.

25 mL of Schlumberger A262 corrosion inhibitor is then mixed into the acid solution and stirred using a magnetic stirrer.

Acid samples are collected before and after the addition of corrosion inhibitor, which serves as the initial acid concentration prior to jetting. This is done by taking approximately 10 mL of acid from the acid tank using a plastic pipette and placing it in a 30 mL glass sample bottle with the proper label. Acid samples are then be collected after every jetting stage, and subsequent titration analyses are performed to monitor the change in concentration.

It is also necessary to set the pulse pump prior to jetting at the right flow setting in order to achieve the desired jetting velocity. This is done by adjusting the capacity of the

pump to the proper percentage of its maximum capacity such that the velocity of the fluid coming out of the nozzle corresponds to the desired value. The percentage is calculated using the pump flow rate (q_{pump}), the cross-sectional area of the nozzle, and the maximum pump flow rate (q_{max}). To achieve a jetting velocity of 107 ft/s, 48.75% of the maximum pump flow rate is required. The calculation is shown by Equations 2.4 and 2.5 (Holland, 2014).

$$q_{pump} = (q_{max})(\text{capacity }\%) = \left(16.3\ \frac{\text{gal}}{\text{hr}}\right)(0.4875) = 7.946\ \frac{\text{gal}}{\text{hr}} \tag{2.4}$$

$$\left(7.946\ \frac{\text{gal}}{\text{hr}}\right)\left(0.133681\ \frac{\text{ft}^3}{\text{gal}}\right)\left(\frac{1\text{ hr}}{3{,}660\text{ s}}\right) = 2.9506 \times 10^{-4}\ \frac{\text{ft}^3}{\text{s}} \tag{2.5}$$

Calculating the cross-sectional area of the nozzle (A_{nozzle}) with an inner diameter (D_{nozzle}) of 0.0225 inch and computing for the jetting velocity (v_{jet}), the following values are obtained (Equations 2.6 and 2.7):

$$A_{nozzle} = \frac{\pi}{4}D_{nozzle}^2 = \frac{\pi}{4}\left[(0.0225\text{ in})\left(\frac{1\text{ ft}}{12\text{ in}}\right)\right]^2 = 2.7612 \times 10^{-6}\ \text{ft}^2 \tag{2.6}$$

$$v_{jet} = \frac{q_{pump}}{A_{nozzle}} = \frac{2.9506 \times 10^{-4}\ \frac{\text{ft}^3}{\text{s}}}{2.7612 \times 10^{-6}\ \text{ft}^2} = 107\ \frac{\text{ft}}{\text{s}} \tag{2.7}$$

By performing similar calculations, it is determined that 68.50% and 91.50% of the maximum pump flow rate are required to produce jetting velocities of 150 ft/s and 200 ft/s respectively.

The inlet cap is first attached to the inlet side of the main core holder body. The two spacer rings are then inserted from the outlet side by rotating the core holder and letting it fall all the way down the cylinder, ensuring full contact with the surface of the

inlet cap. The saturated core is carefully placed in the core holder, while making sure that the straight line marking previously drawn on the rock is aligned with the marking on the core holder. This is to guarantee that the core is in the same orientation for all stages. The outlet holder is then carefully put in place and securely locked. The fully assembled core holder is rotated to its proper orientation, with the inlet side on top and the outlet side at the bottom.

The tube fittings and connections for the inlet, outlet, and hydraulic oil lines are then connected. With both the entrance and exit hydraulic valves open, and the waste hydraulic oil beaker properly placed, hydraulic oil is pumped until a steady flow is achieved at the exit line. This prompts the closing of the hydraulic oil exit valve followed by the continued pumping of more hydraulic oil until a 750 psi pressure is reached inside the oil sleeves, as indicated by the pressure gauge.

The water accumulator valve, which controls the flow of water from the tank to the pump intake, is then opened. The opening of the waste valve and the acid recycle valve followed, then the pump is started. After water fully fills the system's tubing, which is manifested by a constant steady flow of fluid into the waste accumulator, the pressures in the system are then ready to be controlled to achieve the desired pressure differential across the core. This increase in pressure is performed in 250 psi increments to avoid pressure shock in the system which may potentially damage the equipment. Figure 2.11 shows the setup with all the tubing connections attached.

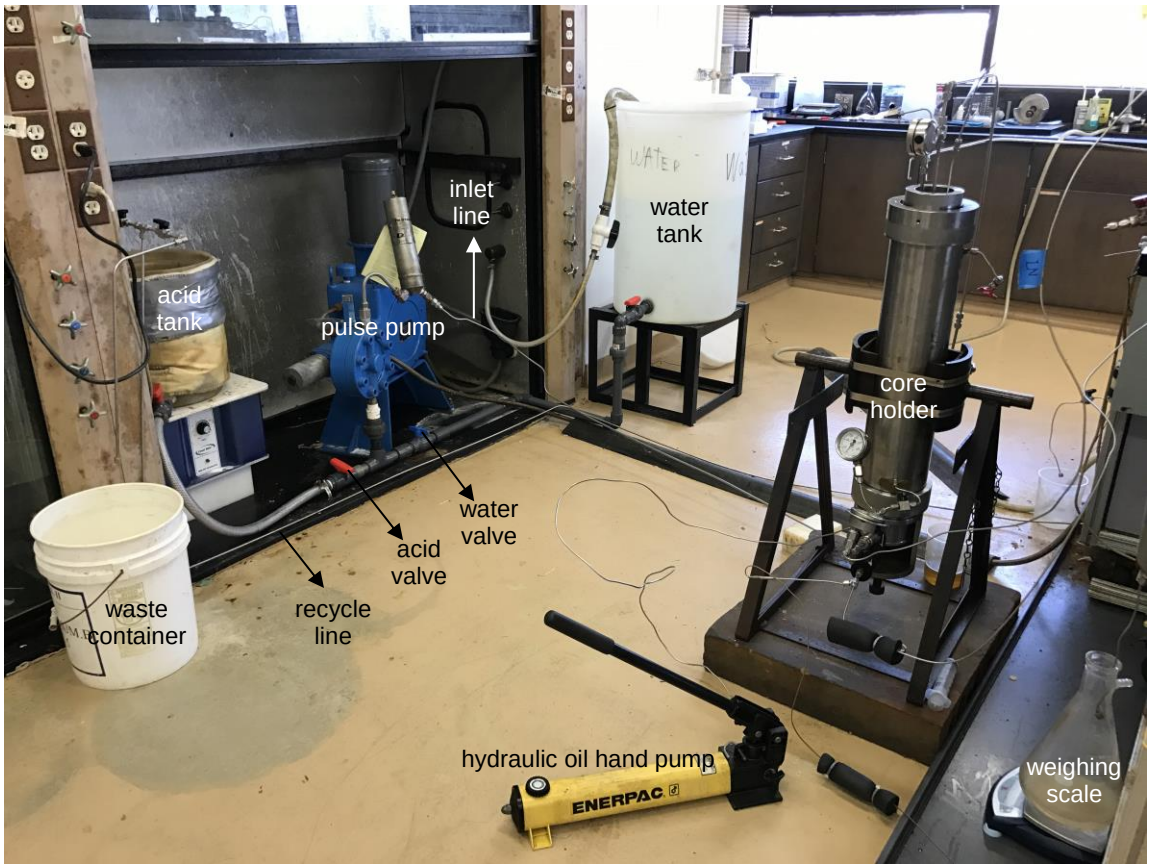

Figure 2.11. Acid jetting setup with all the connections attached.

The nitrogen tank that controls the downstream backpressure is opened until a downstream pressure of 1,000 psi is reached, as shown by the downstream pressure gauge. The upstream backpressure is then set to 250 psi by slowly opening the other nitrogen tank, and more hydraulic oil is pumped until a confining pressure of 1,000 psi is reached. The upstream backpressure is then increased further to 500 psi. After the pressure equalized across the core, as evidenced by a near-zero pressure differential, the confining pressure is increased to 1,500 psi. The upstream backpressure is then increased to 1,000 psi, and the pressure across the core is allowed to equalize. The pressure differential across the core is then ready to be set to the desired value for the stage by further increasing the

upstream pressure until the difference between the upstream and downstream pressure values is equal to the desired pressure differential. The pressure transducer displays this value. It is necessary to ensure that the confining pressure is around 500 psi higher than the upstream value in order to prevent fluids from flowing on the sidewall of the core instead of through it.

The LabView program is subsequently started. The pressure differential across the core is observed through the computer, ensuring that the system is stable and a steady flow is achieved for at least a few minutes. Once stable flow is established, the setup can then be switched from water jetting to acid jetting.

The water accumulator valve is closed as the acid accumulator valve is simultaneous opened. Using a timestamp application (Emerald for iOS) for smartphones, the exact time of this switching is recorded (Figure 2.12). This is labeled as the time the acid valve is opened. Depending on the jetting velocity, it takes a few seconds for the acid to flow from the pump to the nozzle outlet. Using the Bernoulli equation, these times have been determined previously by Holland (2014) to be 32 seconds for a jetting velocity of 107 ft/s, 23 seconds for 150 ft/s, and 17 seconds for 200 ft/s. These numbers are confirmed in the laboratory through timed flow testing. Accounting for these delay times is necessary in the calculation of jetting times to have a more accurate representation of the jetting phenomenon and to standardize the results. The time at which acid reaches the nozzle is the true starting point of the jetting time for a particular stage.

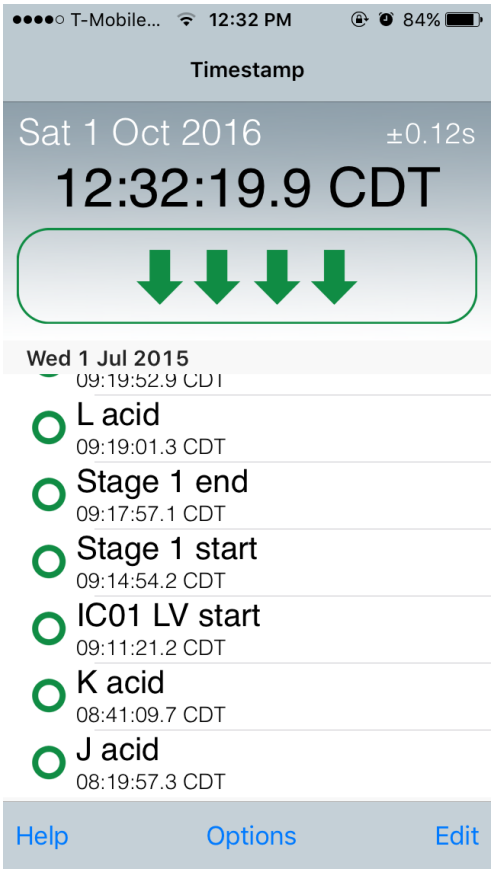

Figure 2.12. Emerald timestamp application for iOS.

Initially, the waste valve in the recycle line is opened while the acid recycle valve remains closed, in order to keep the concentration of the acid in the accumulator as close to the initial 15% as possible. After the recycle stream is determined to have a pH of zero, as indicated by a pH test strip, the acid recycle valve is then opened, and the waste valve closed.

Acid jetting is then allowed to progress for the set jetting time for the particular stage. Once the designed jetting time for the stage is reached or when breakthrough is achieved, the acid accumulator valve is closed simultaneously as the water accumulator

valve is opened. This exact time is recorded through the timestamp application. Again, since it takes a few seconds for the remaining acid to travel from the pump to the nozzle after the system is switched from acid to water jetting, the time water reaches the nozzle is considered as the true end point of a jetting stage. This is true except for the breakthrough stage, where the end point is the time the pressure differential between the outlet and inlet of the core reaches zero.

The acid recycle valve is then closed and the waste valve is opened at the time the switch from acid to water jetting occurs. This is to prevent the dilution of the acid in the accumulator.

Water jetting is allowed to progress until the recycled fluid from the top of the core holder to the waste bucket is determined to be neutral using a pH test strip. Once the recycle stream is determined neutral, the nitrogen tank connected to the upstream backpressure regulator is closed and the upstream backpressure is lowered to 750 psi. The confining pressure is lowered to 1,250 psi and the upstream backpressure is lowered again to 500 psi. The confining pressure and the upstream backpressure are further decreased to 1,000 psi and 250 psi, respectively. Finally, the confining pressure is lowered to 750 psi and the upstream backpressure is lowered to 0 psi.

The pump is stopped and the core holder is disassembled. The core is then carefully removed and its wet weight is recorded.

A small sample of fluid (around 10 mL) is taken out of the acid solution container at the end of each stage, and stored in a small glass bottle. These are saved for subsequent titration analyses.

CT scan images of the core are then obtained using an X-ray CT machine (Toshiba Aquilion TSX-101A/RG). The core is placed on the scanner bed (Figure 2.13) in such a way that the straight line drawn on its side overlaps the laser projection of the scanner. This is to guarantee that the core is scanned as vertically straight as possible. It also functioned as a way to ensure that the core is consistently scanned in the same manner throughout the acid jetting stages, which enabled the straightforward juxtaposition of the CT images for the analyses.

After the CT scan for the jetting stage, the core is then put back in the core holder for the subsequent acid jetting stage. It is necessary to put the core back in the core holder at exactly the same orientation as it is placed previously to ensure consistency. The marker lines drawn on the cores are used during this step. The same pressure differential is applied across the core during the succeeding jetting stages.

This process of acid jetting and CT scanning is repeated for all the six Indiana limestone cores, until the breakthrough stage for each test is achieved.

The concentrations of the acid samples collected after each stage are then measured through acid-base titration.

Two drops of phenolphthalein indicator solution is added to the HCl samples prior to titration. The gross weight of the bottle before and after the addition of the indicator are recorded. A 30% by weight potassium hydroxide (KOH) solution is prepared and is used to neutralize the acid samples. Using a pipette, drops of the base solution are added until the endpoint is reached, manifested by the solution completely turning light pink. The weight of the neutralized sample is then recorded.

Knowing the empty bottle weight and using subtraction, the weights of the original HCl solution and the added KOH solution are determined. The volumes of the acid and base samples in each glass bottle are then calculated using their known densities. Finally the concentration of the HCl samples are then determined using molar balance, given that the concentration of the KOH solution used is 30%.

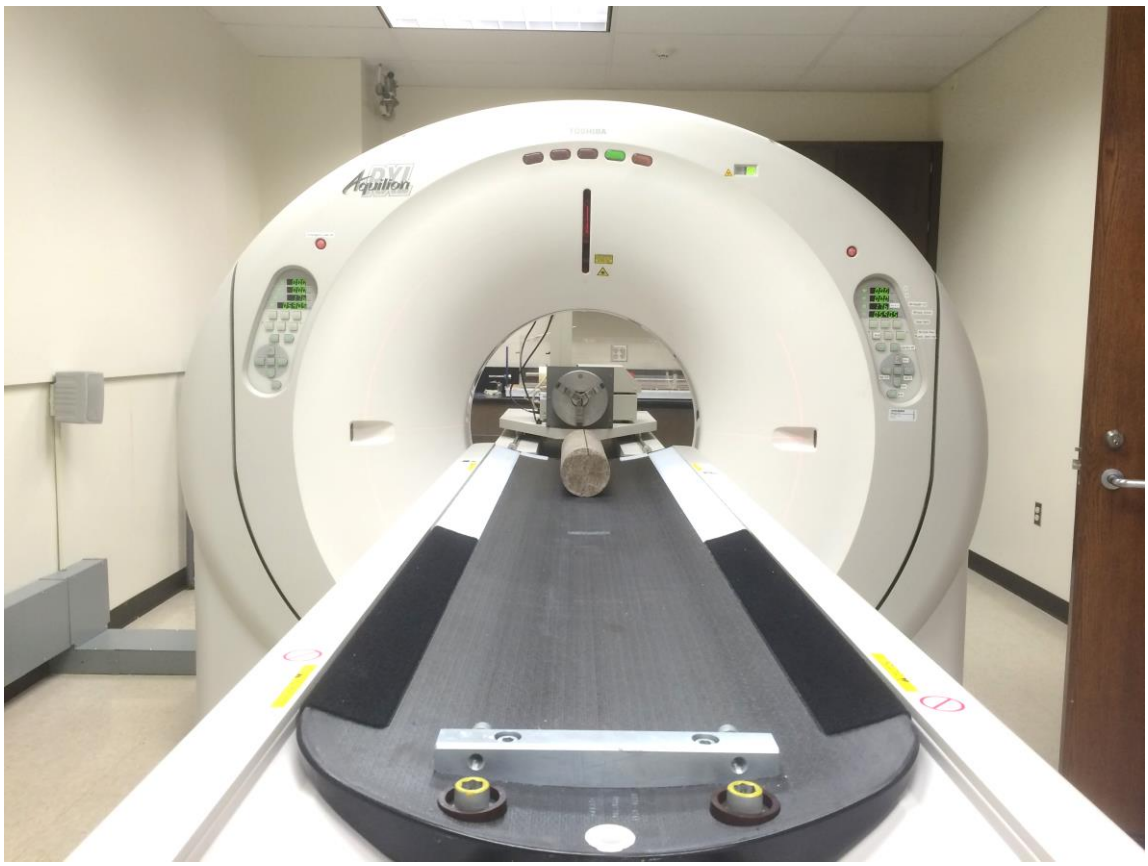

Figure 2.13. Toshiba Aquilion CT scan machine.

2.3 CT Image Processing

CT scan images of the core are produced as raw DICOM (Digital Imaging and Communications in Medicine) files. These can be regarded as hundreds of cross-sectional thin slice images of the core parallel to one other, which provide a digital recreation of the core and its dissolution structures when integrated and processed. Each thin slice image is composed of pixels and each of these pixels has a numeric value that corresponds to the density of the objects that underwent X-ray CT scanning. Low-density materials have low, negative pixel values, and they appear as black pixels in raw CT images. On the other hand, high-density materials have high, positive pixel values, and they appear as white pixels in raw CT images (Seletchi and Duliu, 2007). Therefore, when looking at CT images of core samples, the white and light gray pixels represent the undissolved rock, while the black pixels within the core cross-sectional area represent the dissolution structures.

Since CT imaging is typically used in the medical field, most CT image viewing and processing software are geared towards medical purposes. It is therefore necessary to appropriate these computer programs for rock analyses. In this study, the Mac OS-based image processing software OsiriX Lite (Figure 2.14) and Horos (Figure 2.15) are used for the analyses and processing of the DICOM files. The two are very similar in terms of functionality and general software design, and both are intended for medical use. Nonetheless, utilizing them to study dissolution structures in rocks is a straightforward process. OsiriX Lite is the 32-bit free version of the more powerful 64-bit software OsiriX

MD. On the other hand, Horos is an open-source 64-bit free CT image viewer and it is based upon OsiriX and other open source software.

Because of its extensive file library features, OsiriX Lite is used for CT image database management and the selection of the image series to be processed in this study. However, OsiriX Lite does not allow processing of CT data with more than 500 image series. This limitation is significant as the sets in this study go up to around 1,400 images and this makes OsiriX Lite unsuitable for 3D image processing. Therefore for the purposes of pre-processing and processing of the CT data in this study, the more powerful Horos is used.

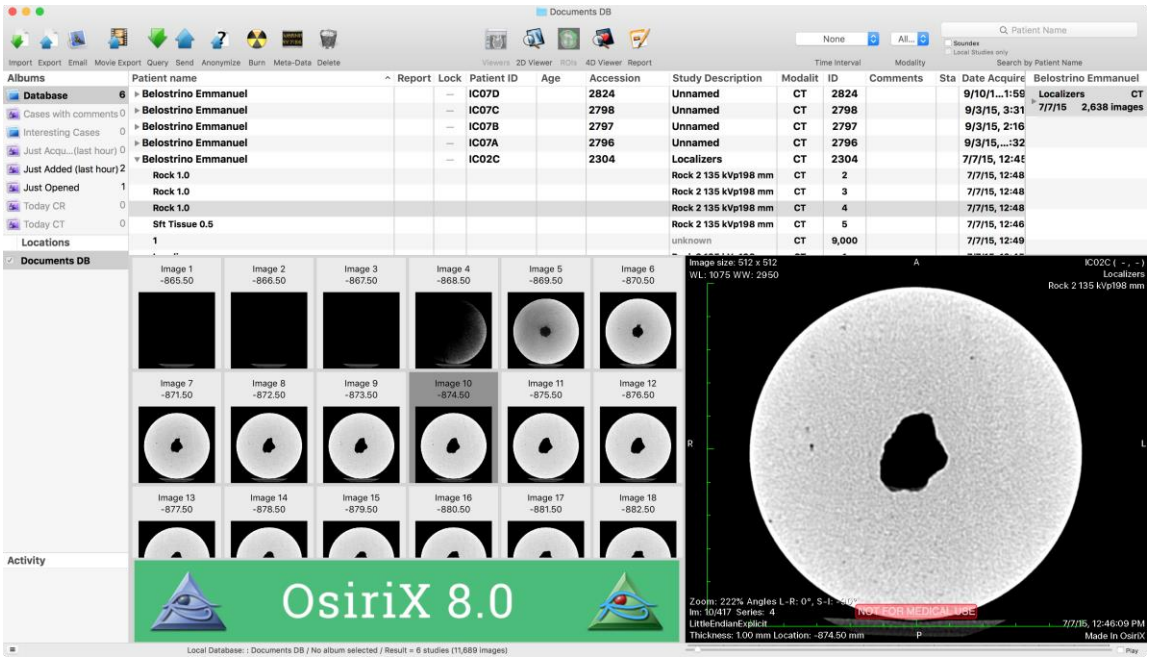

Figure 2.14. OsiriX database screen.

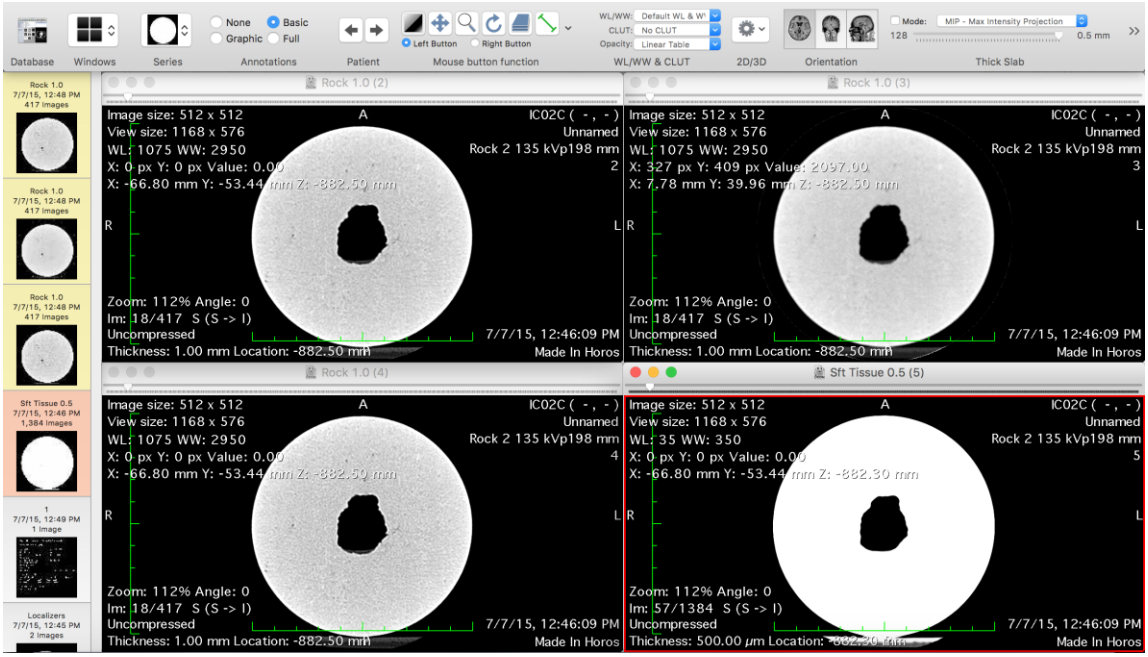

Figure 2.15. Four sets of CT images viewed using Horos.

The CT scan machine used in the study outputs four sets of core images of varying contrast, resolution, and focus (Figure 2.14). The first three sets are image slices taken every 1 millimeter along the core, and the images have higher resolution and lower contrast. On the other hand, the fourth image set is taken every 1/3 millimeter slice consisting of image slices with lower resolution and higher contrast.

For the purposes of visualization and wormhole analysis, the sets with higher resolution images are used as they provide higher levels of detail, which allow the rendering of even the tiniest of wormhole branches. Among the three high resolution image sets, the one with the best focus is selected as it provides the highest level of clarity. On the contrary, cavity volume calculation is more accurately performed using the fourth image set with higher contrast and greater number of image slices. The reason is that it

more easily distinguishes the cavity boundaries due to the high contrast, and it provides more image slices of cross-sectional areas used for volume integration, which yields greater accuracy.

Pre-processing of the DICOM files is necessary before generating 3D renderings of the cavity and wormholes. The outlying images that are not part of the core are deleted using OsiriX Lite prior to loading them on Horos. Using the oval selector tool in Horos, the region of interest for each thin slice is specified within the cross-sectional area of the core. The pixel values of the empty space outside the region of interest is set to the highest level of whiteness (3024) to remove image noise and to allow better visualization (Figure 2.16).

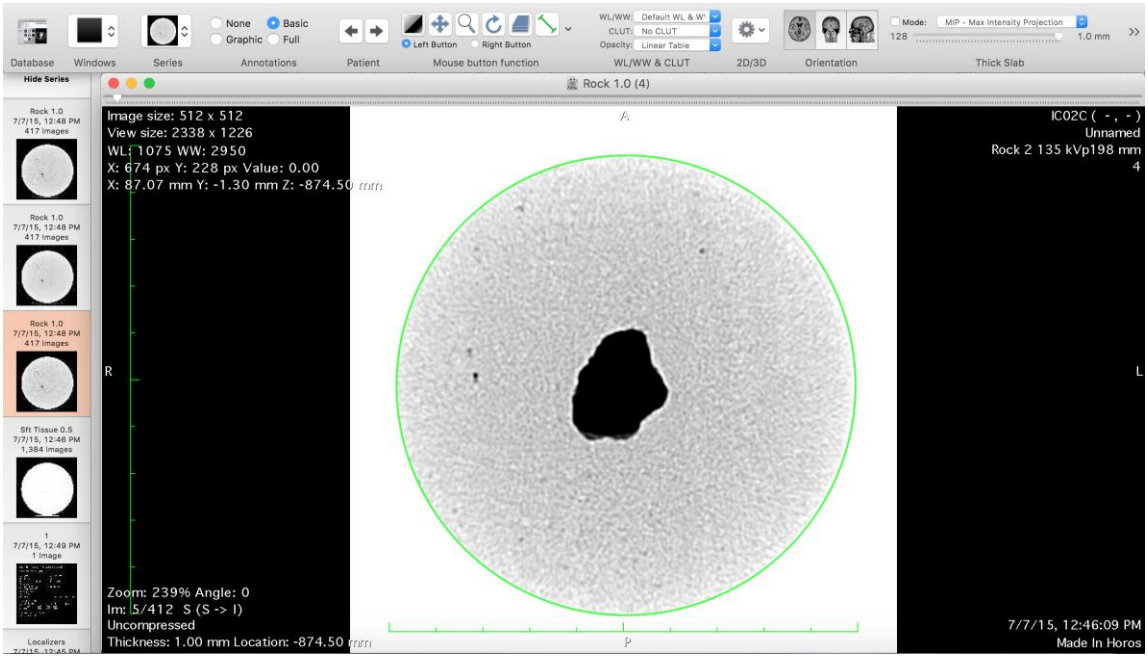

Figure 2.16. Pre-processing of CT images.

The 3D volume rendering functionality of Horos is then utilized to process the images and to visualize the dissolution structures. For clearer visualization and image generation, the 16-bit color look-up table editor is used (Figure 2.17). This function generates a distribution plot of all the pixel values contained within the rendered 3D image, and it allows the editing of the color and the opacity of the pixels. Since the image set is pre-processed, the pixel value distribution plot creates a clear divide and makes it apparent where the dissolution structures with low pixel values are (left peak) and where the undissolved rock with high pixel values are (right peak). The opacity of the undissolved rock pixels are lowered down to zero, while those of the dissolution structures is set to 100%. In addition, the color of the dissolution structures is changed to white for a clearer visualization against the black background.

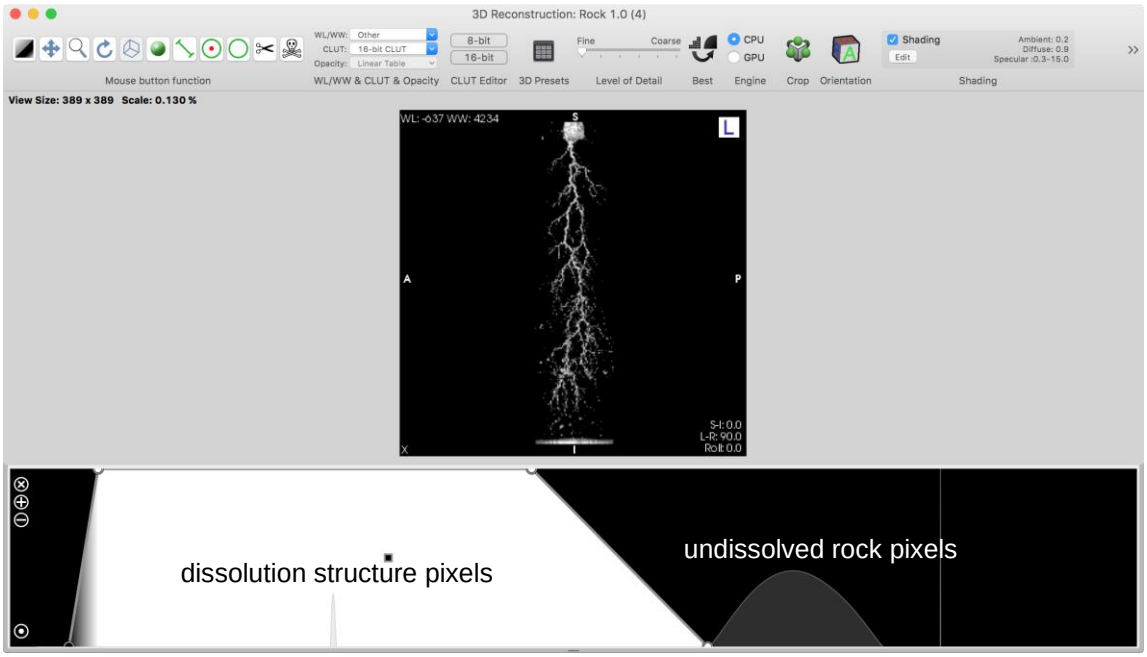

Figure 2.17. 3D volume rendering of the dissolution structures.

Through the built-in functions of Horos, the wormhole length and cavity volume for each jetting stage are measured (Figures 2.17 and 2.18). Wormhole length is measured from the top surface of the core facing the nozzle to the lowermost wormhole branch. Horos calculates the cavity volume by integrating the cross-sectional areas of each thin slice image that are part of the cavity. For consistency, it is necessary to define the point where the cavity ends and the wormhole starts. This is achieved by setting the minimum cavity area to be 12.57 mm^2, which corresponds to a wormhole with a diameter of 4 mm, and thereby serves as the endpoint of the area integration for the cavity volume calculation.

The high-definition capabilities of the software and the consistent image processing parameters used ensure that the visualization and measurement of the dissolution structures are consistent and repeatable.

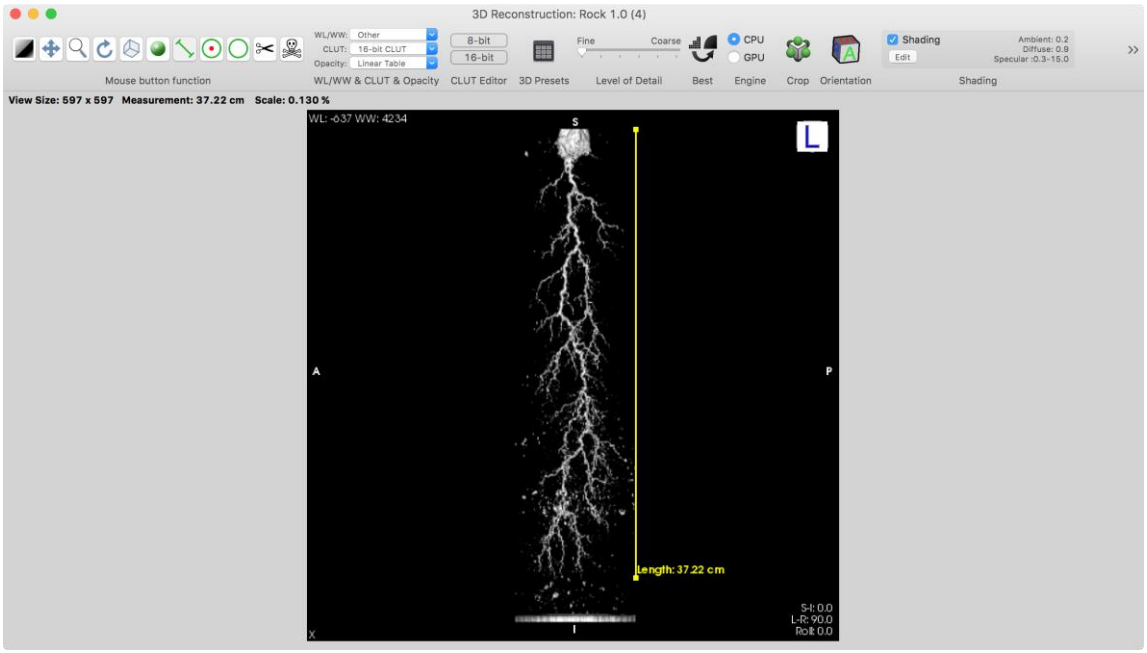

Figure 2.17. Wormhole length calculation.

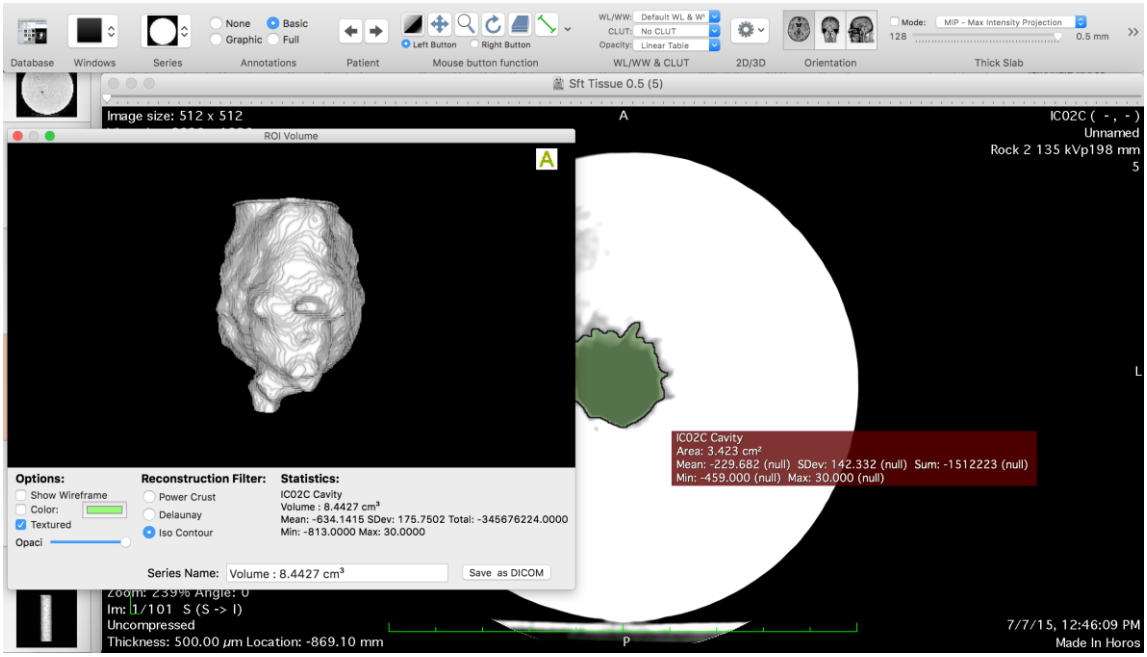

Figure 2.18. Cavity volume calculation through cross-sectional area integration.

Horos also has the capability to produce video files of the dissolution structures rotating around the central axis of the core, which provides a good visualization of the cavity and the wormhole from multiple vantage points. Using Adobe After Effects CS6, these video files for the jetting stages of each core are then juxtaposed against one another in succession to visualize the progression of the dissolution structures created during acid jetting.

3. RESULTS AND DISCUSSION

The primary data collected and analyzed for this study can be classified into two: (1) experimental data collected during the experimental procedure (data from LabView and acid samples), and (2) digital CT data collected after each stage.

Table 3.1 shows the measured properties of the six Indiana limestone cores after water saturation and permeability testing. The porosities (ϕ) of the samples range from 14.4% to 15.1%, while the permeability (k) values ranged from 2.43 mD to 6.87 mD. The experiments are set to be performed at three acid jetting velocities (v_{jet}) of 107 ft/s, 150 ft/s, and 200 ft/s. For each jetting velocity, two cores are used – one with a higher permeability (around 4 mD to 7 mD), and one with a lower permeability (around 2 mD to 3 mD). The required pressure differentials (ΔP) across the core are calculated using Darcy's equation (Equation 2.3), with the initial interstitial velocity set at 0.5 cm/min. The interstitial velocities (v_i) throughout the stages are then expected to average around 1 cm/min, as previous experiments have demonstrated (Holland, 2014; Ndonhong, 2014). This standardized average interstitial velocity then allows proper comparison of the results.

Table 3.1. Core preparation results summary.

	Core ID	k (mD)	ϕ	Desired ΔP (psi)	v_{jet} (ft/s)
1	IC01	4.01	14.6%	180	107
2	IC02	2.43	14.3%	290	107
3	IC03	6.87	15.1%	110	150
4	IC05	2.38	14.7%	140	150
5	IC04	5.30	14.4%	300	200
6	IC06	3.53	14.4%	200	200

3.1 Average Interstitial Velocity Calculation

It is necessary to calculate the effluent flow rate (q_{effluent}) throughout the stages for each core in order to determine the average interstitial velocity. This is done using the summation of all the effluent weight differences after each stage ($\Delta W_{\text{effluent}}$), the jetting time for each stage (Δt_{stage}), and water density (ρ_w), as shown by Equation 3.1 (n is the number of jetting stages). The effluent weight difference data are collected and recorded every second by the LabView program, along with their respective times.

$$q_{\text{effluent}} = \frac{\sum_{i=1}^{n} \Delta W_{\text{effluent},i}}{\left(\sum_{i=1}^{n} \Delta t_{\text{stage},i}\right)\rho_w} \tag{3.1}$$

Interstitial velocity (v_i) is the flow rate through the porous rock cross-sectional area. The flux equation is described by the Equation 3.2:

$$v_i = \frac{q}{A\phi} \tag{3.2}$$

where q is the flowrate through the core, A is the core cross-sectional area, and ϕ is porosity. Assuming steady state flow, the effluent flow rate can be substituted in the equation above to calculate the average interstitial velocity.

The average interstitial velocity for each core is shown in Table 3.2. The initial values are set at around 0.5 cm/min, which then averaged to around 1 cm/min after the breakthrough stage. The values were all within reasonable range, enabling justifiable comparison of the experimental results.

Table 3.2 also shows the cumulative jetting time and the number of stages for each rock sample. Cumulative jetting time ranges between 5.58 and 11.15 minutes, while the number of stages performed is between 3 and 6 for each core, for a total of 26 acid jetting experiments performed throughout the study. Figures A.1 and A.2 in the appendix shows images of the core samples after multi-stage acid jetting.

Figure A.3 in the appendix shows a screenshot of the Excel file that processes the experimental results, while Figures A.4 to A.9 show the pressure and weight data collected as multi-stage acid jetting progressed for each rock sample.

Table 3.2. Experimental parameters and interstitial velocity.

	k (mD)	v_{jet} (ft/s)	initial v_i (cm/min)	ave v_i (cm/min)	cumulative jetting time (min)	no. of stages
1	4.01	107	0.56	1.29	9.30	3
2	2.43	107	0.50	1.62	7.23	4
3	6.87	150	0.50	1.38	8.22	4
4	2.38	150	0.53	0.98	5.58	4
5	5.30	200	0.49	1.22	11.15	6
6	3.53	200	0.49	1.36	8.40	5

Using the data collected from the LabView program, the average interstitial velocity for each jetting stage of every rock sample is calculated. This information provides an overview of how the interstitial velocity increases as jetting time progresses. The results are shown in Figure 3.1. Interstitial velocity increases slowly during the initial stages, followed by a dramatic increase during the breakthrough stage.

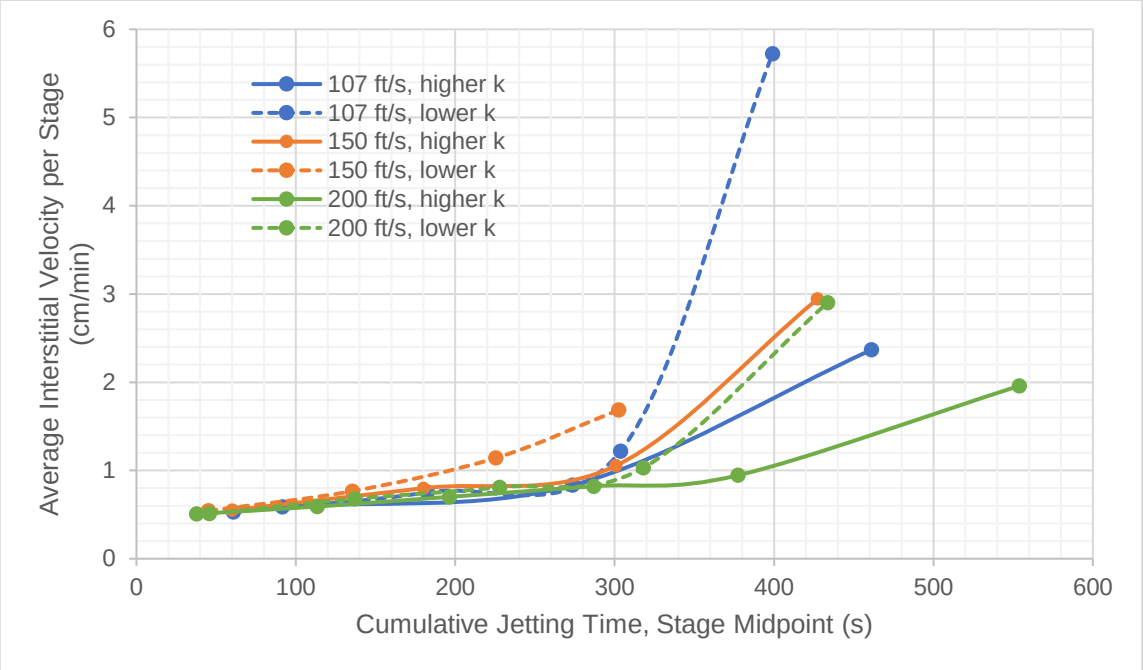

Figure 3.1. Average interstitial velocity per stage.

The breakthrough stage can be considered as an outlier point as it leads to significantly higher flowrates, which translates to very high interstitial velocities. Moreover, it is certain than only Darcy flow occurs during the earlier stages, while there is a possibility of non-Darcy flow being accounted for during the breakthrough stage. Figure 3.2 shows the average interstitial velocity per stage, without the breakthrough stage. A more linearly increasing trend is observed.

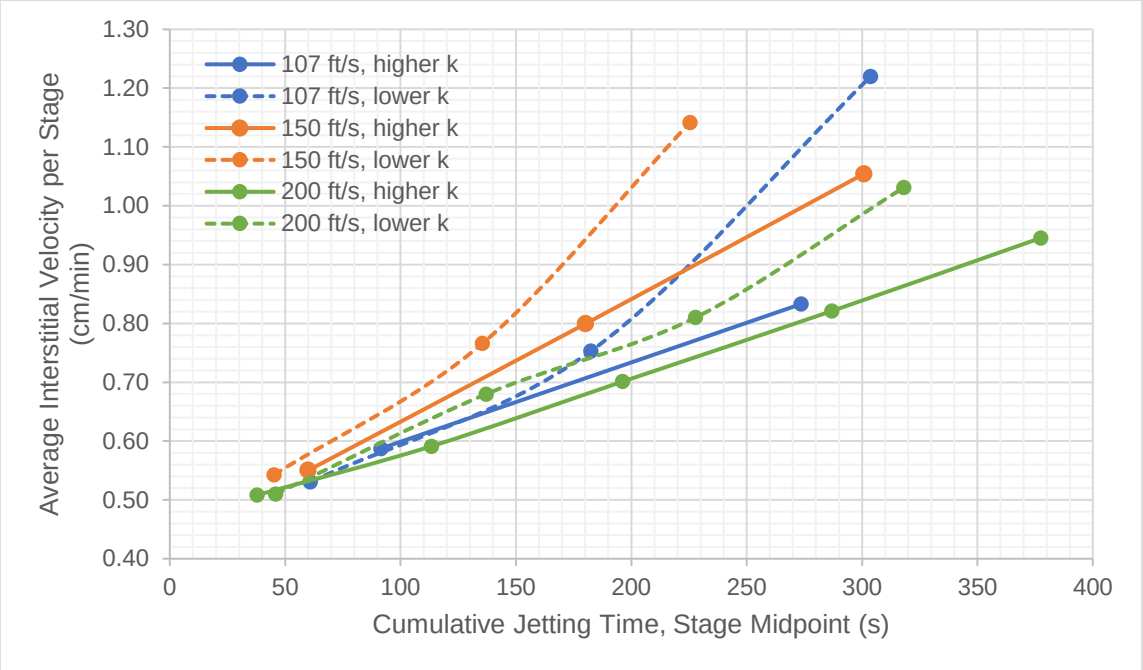

Figure 3.2. Average interstitial velocity per stage (breakthrough stage considered as outlier).

Wormhole growth is dependent on interstitial velocity (Buijse and Glasbergen, 2005). Ideally, interstitial velocity is held constant throughout the experiments, like in matrix acidizing, to justifiably draw observations on multi-staged wormhole growth. When performing matrix acidizing laboratory studies, the flux through the core is maintained constant throughout the experiment, as the differential pressure between the inlet and outlet lines is allowed to gradually decrease until breakthrough is achieved (Dong et al., 2012). On the other hand, acid jetting experiments have constant pressure differentials through the core due to the presence of upstream and downstream backpressure regulators and a recycle line. Hence, using the current acid jetting experimental setup, instantaneous interstitial velocity increases as dissolution structures develop. These results illustrate how investigating the wormhole growth and growth rates

is challenging for multi-stage acid jetting experiments. This limitation will be discussed further in the succeeding sections.

3.2 Acid Concentration Analysis

Figure 3.3 shows the measured acid concentrations before performing the experiments and after each jetting stage.

Because of titration design limitations, the initial acid concentrations measured are higher than 15%. The samples were not diluted prior to titration, and the base solution used had too high of a concentration at 30%. This lead to over-titration, yielding higher concentrations of acid calculated.

The results show a consistent decline in acid concentration since spent acid is recycled back to the acid container as jetting progressed. The decline ranges from around 4% to 6%, and experiments that had a longer breakthrough time resulted in a larger decline in acid concentration.

The ideal experiment scenario is to have constant acid concentrations throughout the experiment in order to achieve better experiment control and more consistent and standard results. However, this requires significantly more acid solution to be prepared and the elimination of the acid recycle stream.

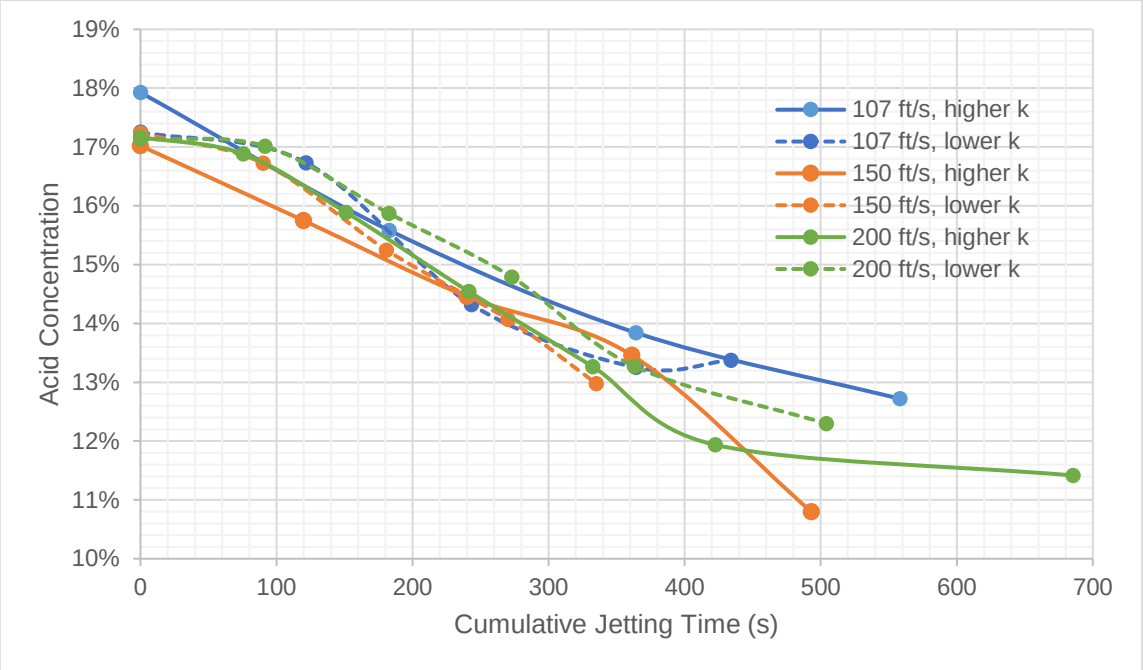

Figure 3.3. Acid concentration as jetting progressed.

3.3 CT Image Processing Results

Tables A.1 to A.6 in the appendix show the measurements and calculations obtained after processing the CT scan images from multi-stage acid jetting. Cavity volume and wormhole length are calculated using Horos.

Figures 3.4 to 3.9 show the development of dissolution structures through time. By side-by-side comparison of the rendered 3D images of the dissolution structures as acid jetting progressed, clear snapshots of the formation of the cavities and wormholes are observed. The results successfully show that during experimental acid jetting, the cavity and wormhole grow simultaneously. This revelation provides the answer to the most important question of this study. Although this concurrent growth has been previously hypothesized (Beckham et al., 2015), these images are the first to confirm and illustrate

this phenomenon. This finding plays a significant role in modeling and simulating acid jetting. A dynamic model that combines the concurrent growth of cavity and wormholes is therefore necessary.

The results illustrate how the cavity grows both radially and along the length of the core. The dynamic images also show how the wormhole propagates from the lowermost tip of the dominant branch, with very minimal growth on the non-dominant branches.

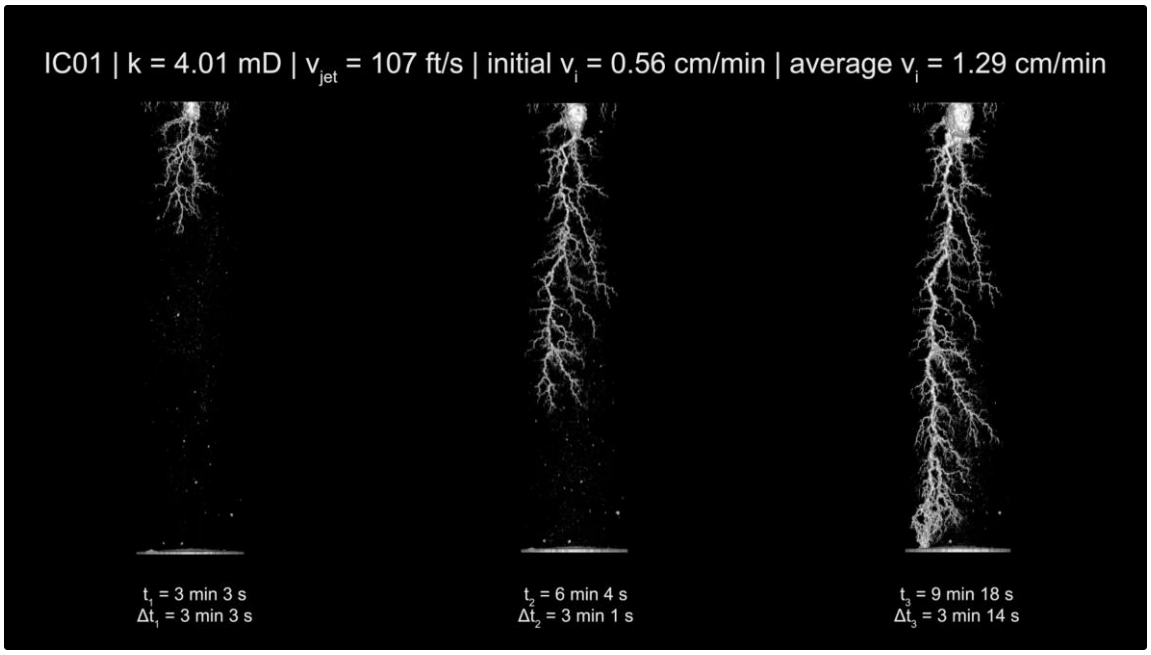

Figure 3.4. IC01 (107 ft/s, higher *k*) acid jetting dissolution through time.

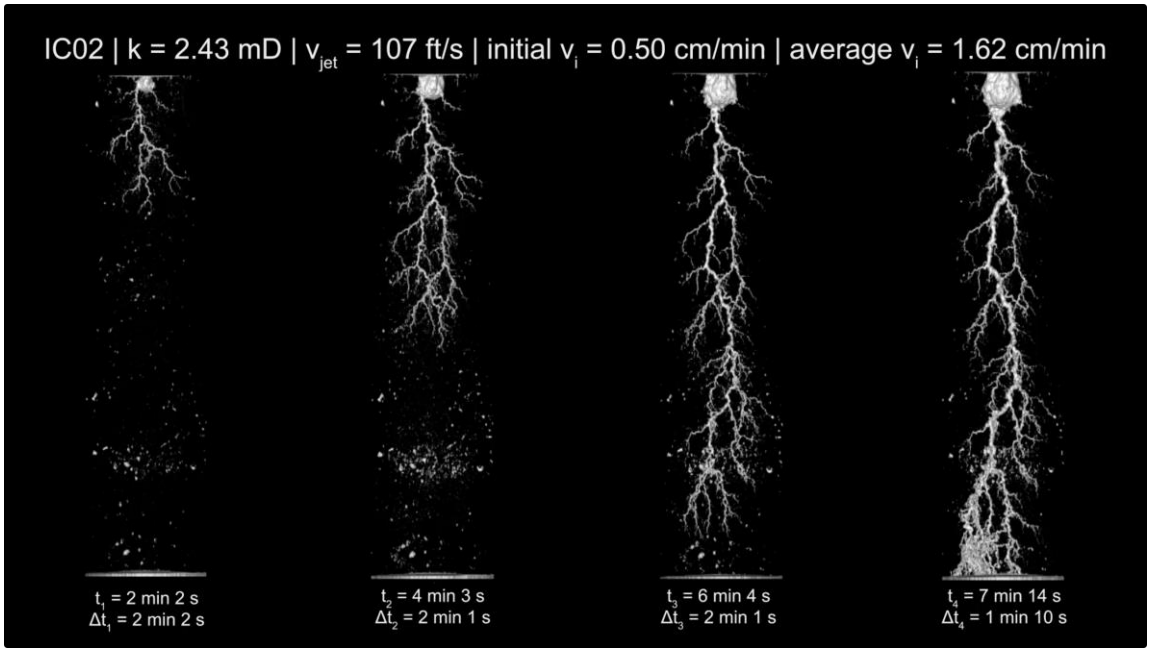

Figure 3.5. IC02 (107 ft/s, lower *k*) acid jetting dissolution through time.

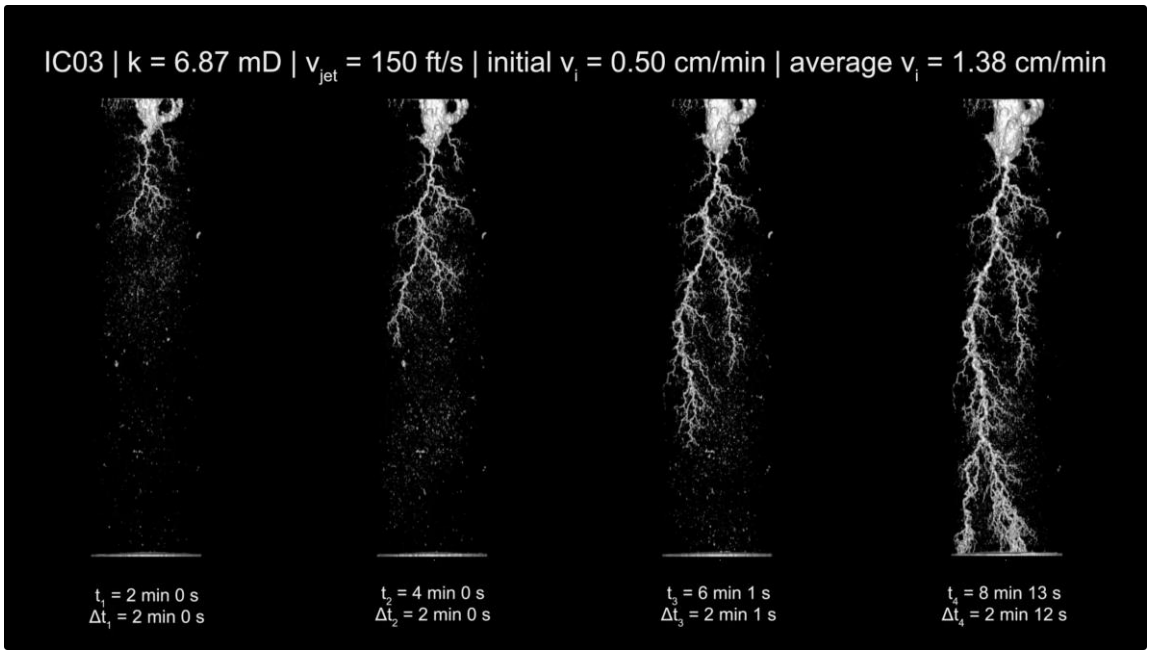

Figure 3.6. IC03 (150 ft/s, higher *k*) acid jetting dissolution through time.

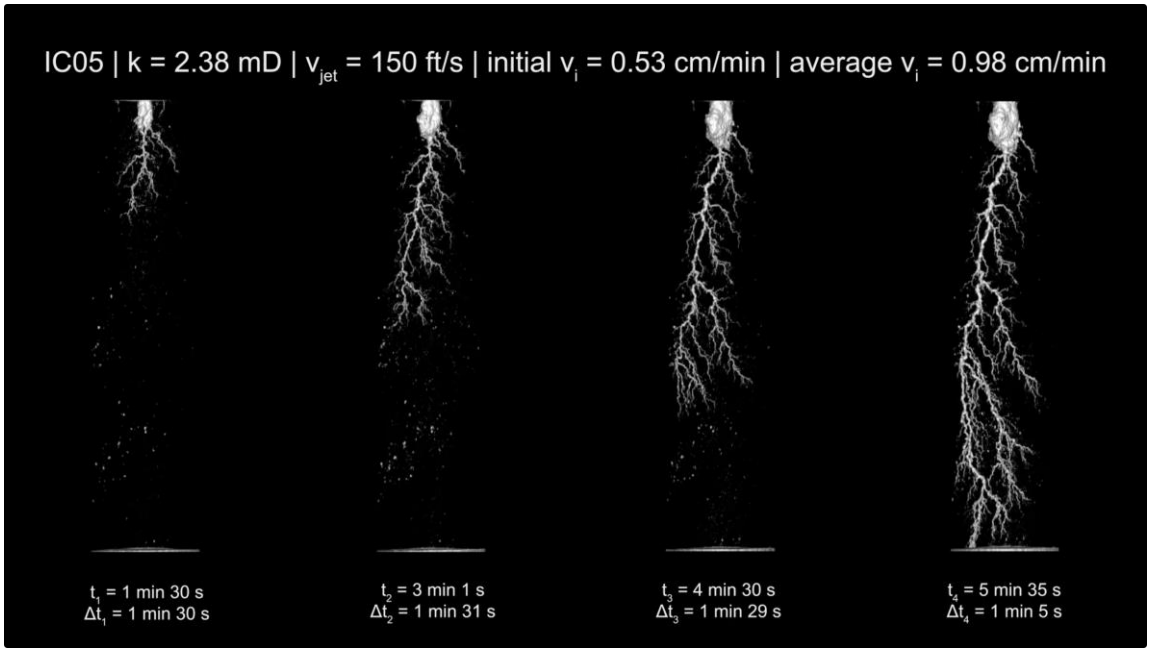

Figure 3.7. IC05 (150 ft/s, lower *k*) acid jetting dissolution through time.

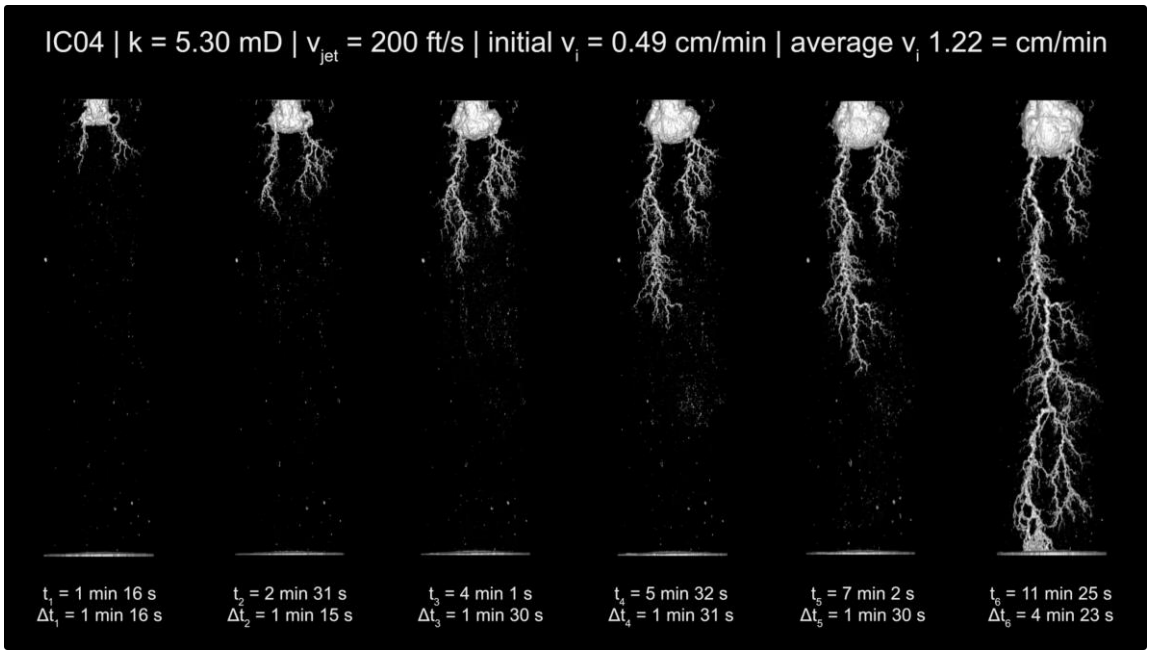

Figure 3.8. IC04 (200 ft/s, higher *k*) acid jetting dissolution through time.

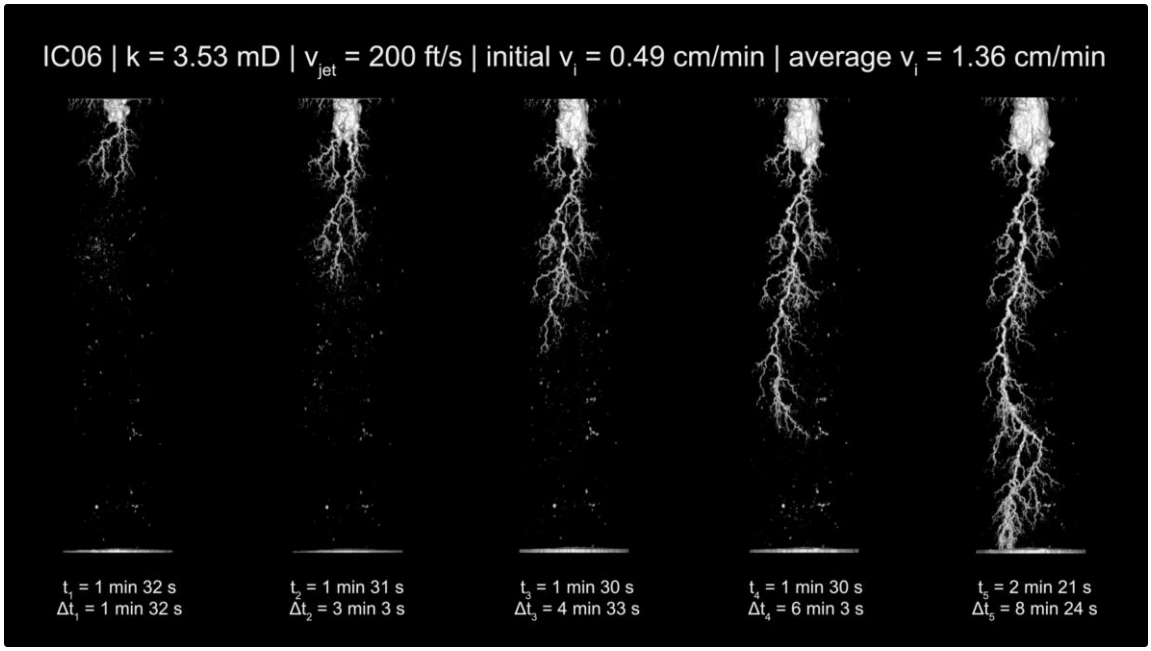

Figure 3.9. IC06 (200 ft/s, lower *k*) acid jetting dissolution through time.

3.4 Wormhole Growth and Growth Rates

Figure 3.10 shows the wormhole length formed in each core as the stages of acid jetting progressed. The curves with blue lines represent cores that underwent jetting with a velocity of 107 ft/s, while the orange lines represent 150 ft/s, and the green lines represent 200 ft/s. The curves with solid lines represent higher permeability cores and the dashed lines represent lower permeability cores. The graph shows that higher permeability cores take longer times to breakthrough, which is consistent with the results observed for matrix acidizing (Etten et al., 2015). Moreover comparing the cores with similar permeabilities, the one with a jetting velocity of 150 ft/s has the shortest breakthrough time followed by 107 ft/s, and 200 ft/s.

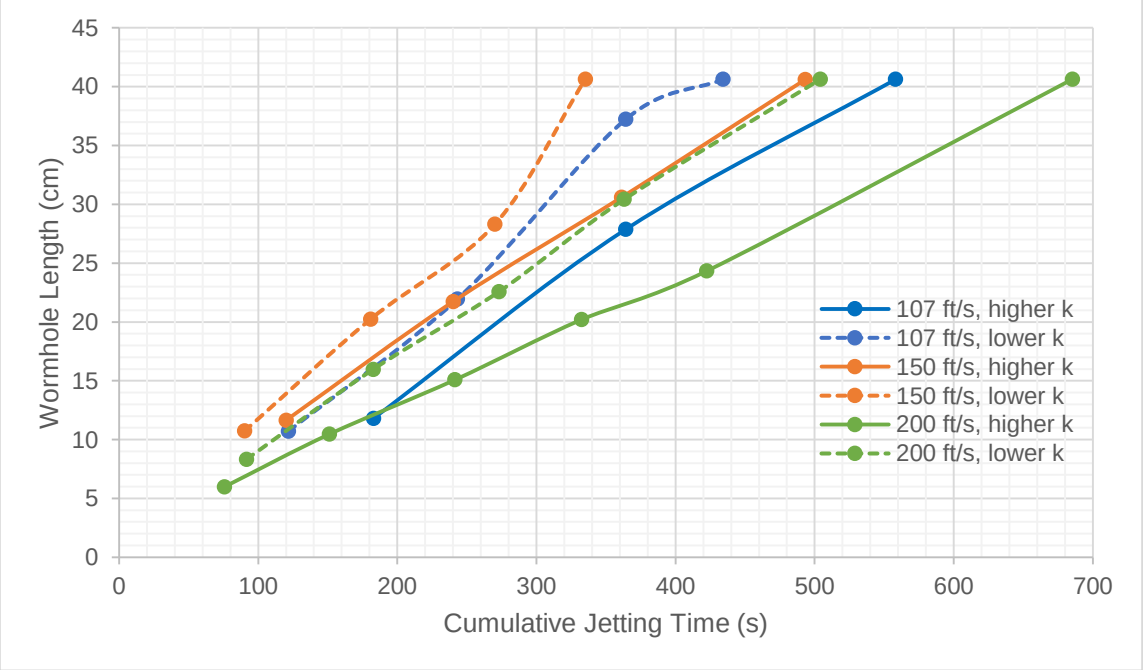

Figure 3.10. Wormhole length versus cumulative jetting time.

To study the wormhole growth rate through time, the derivative of the plot of wormhole length versus time is calculated (Equation 3.3). This is done by dividing the increment of the wormhole length ($\Delta L_{\text{wormhole}}$) by the jetting time for each stage (Δt_{stage}):

$$\text{wormhole growth rate} = \frac{\Delta L_{\text{wormhole}}}{\Delta t_{\text{stage}}} \tag{3.3}$$

Figure 3.11 shows this derivative plot. No conclusive trend regarding wormhole growth rate per stage is observed from the results of the multi-stage acid jetting experiments. This result can be attributed to the imperfect control of the experimental parameters, specifically the variations in the instantaneous interstitial velocities, and the effects of residual acid reacting with the rock after the switch from acid jetting to water jetting at the end of each stage.

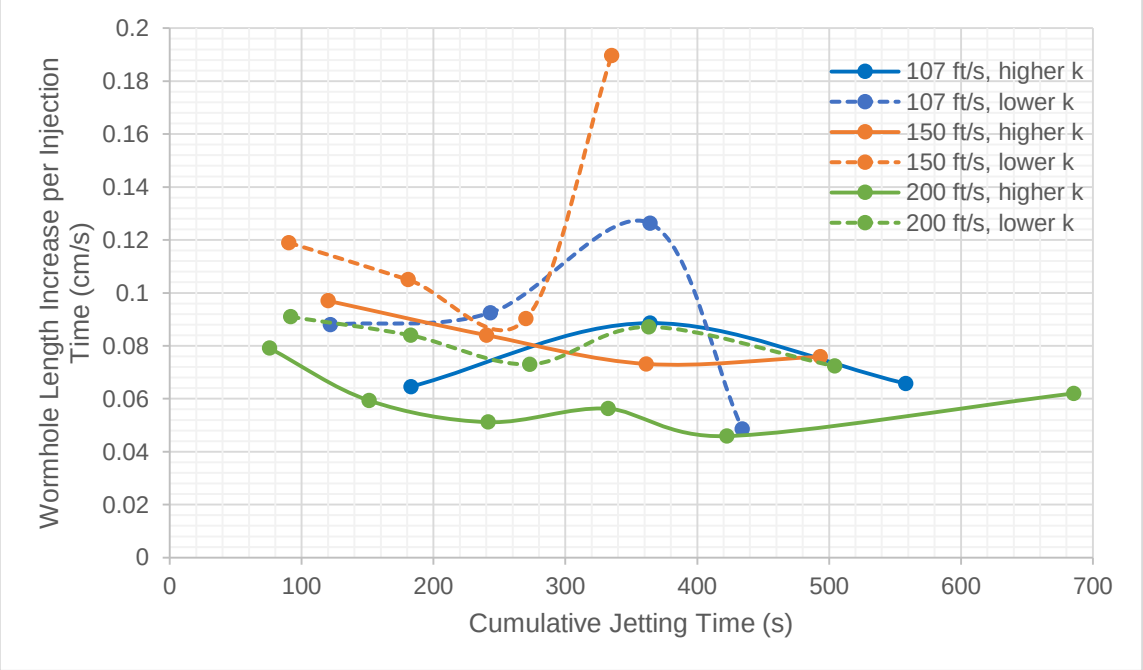

Figure 3.11. Wormhole growth rate per stage versus cumulative jetting time.

These results further highlight the complexity of analyzing acid jetting wormhole growth when the interstitial velocity cannot be directly controlled, as Holland's (2014) results have similarly shown. The current experiment setup does not have the ability to control instantaneous interstitial velocity. This limitation does not only restrict effective comparison of results among jetting experiments, it also hinders the comparison of acid jetting and matrix acidizing experiments, which has constant interstitial velocity throughout. Addressing this issue by the addition of a flow control system in the future iterations of the experiment setup can potentially yield better results and analyses.

At the end of each stage, residual acid is left in the dissolution structures and adjacent pore spaces when switching from acid jetting to water jetting. This residual and dilute acid can still propagate wormholes. This issue, along with the decrease in acid concentration calculated after titration, illustrates another limitation of the current experimental setup and procedure.

In addition to the wormhole growth rate per stage, an average growth rate for each rock sample during the entire jetting procedure can be calculated by linear regression. Fitting a linear trend line on the wormhole length versus time plots yields a slope that corresponds to the average wormhole growth rate for each of the cores. Figures 3.12 to 3.14 show the trend lines and their corresponding equations and R^2 values. Table 3.3 summarizes the results. The observed trends are similar to the trends in breakthrough times. Lower permeability rocks have faster wormhole growth rates. Jetting at 150 ft/s gives the highest wormhole growth rates, followed by 107 ft/s and 200 ft/s. All R^2 values are above 0.98, indicating good linear regression fit.

Table 3.3. Average wormhole growth rates for each rock sample, calculated through linear regression.

	Core ID	*k* (mD)	v_{jet} (ft/s)	ave wormhole growth rate (cm/s)	R^2
1	IC01	4.01	107	0.0732	0.9923
2	IC02	2.43	107	0.0958	0.9958
3	IC03	6.87	150	0.0846	0.9874
4	IC05	2.38	150	0.1145	0.9945
5	IC04	5.30	200	0.0598	0.9977
6	IC06	3.53	200	0.0824	0.9949

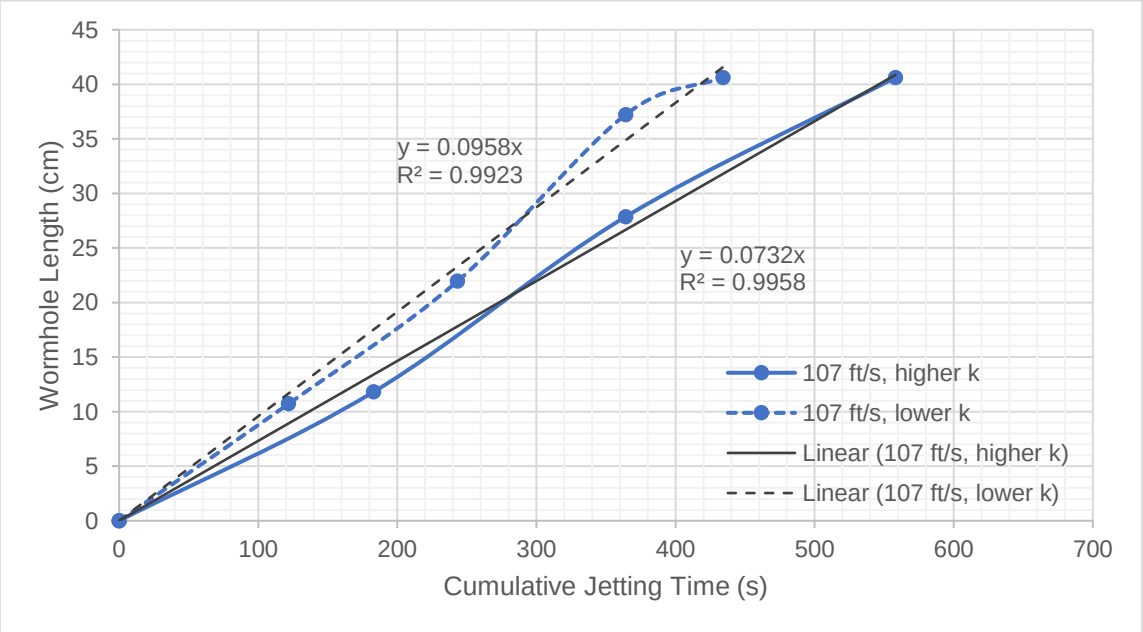

Figure 3.12. Average wormhole growth rate calculation through linear regression (v_{jet} = 107 ft/s).

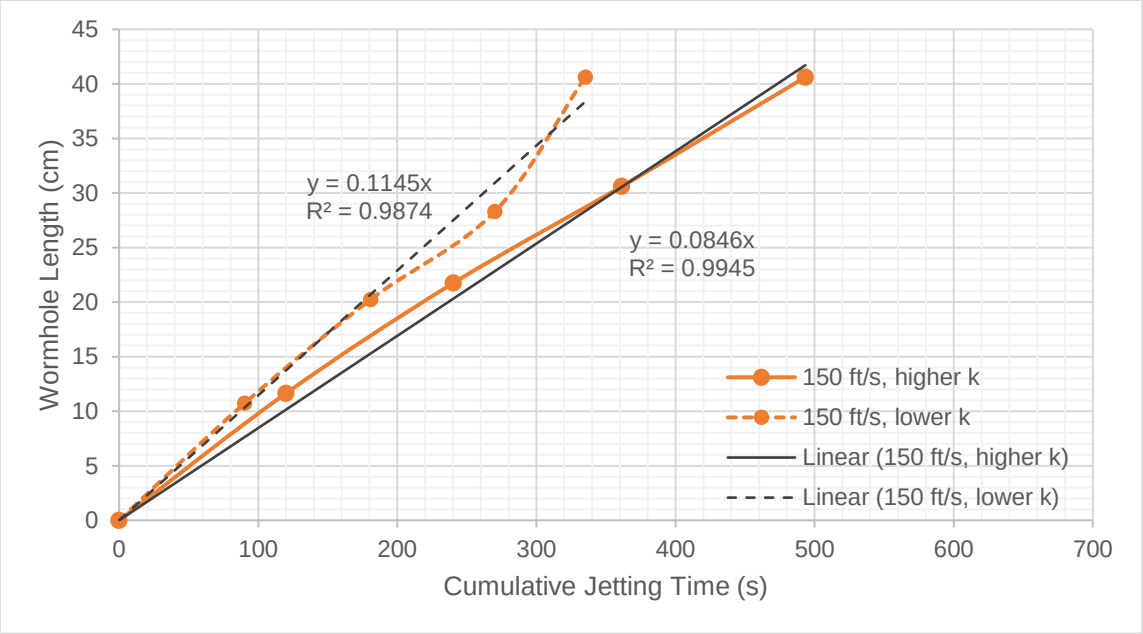

Figure 3.13. Average wormhole growth rate calculation through linear regression (v_{jet} = 150 ft/s).

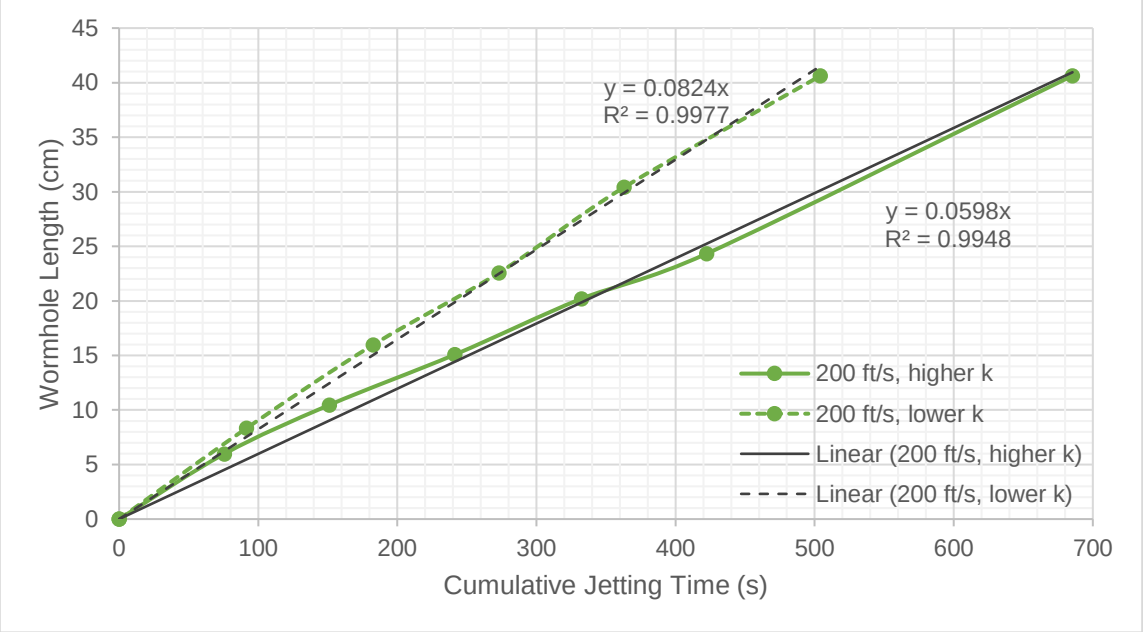

Figure 3.14. Average wormhole growth rate calculation through linear regression (v_{jet} = 200 ft/s).

3.5 Cavity Growth and Growth Rates

The plot of cavity volumes measured as the jetting stages progressed is shown in Figure 3.15. The cavity volumes increase linearly as a function of jetting time, despite the variably increasing interstitial velocity. This result further proves that cavity growth is a stronger function of jetting velocity than interstitial velocity (Ndonhong, et al., 2016).

The trend also indicates that cores with higher permeabilities formed larger cavities, for a constant interstitial velocity. In addition, larger cavities are formed using higher jetting velocities.

Similarly, dividing the increment of the cavity volume (ΔV_{cavity}) by the jetting time for each stage yields the cavity growth rate, as shown by Equation 3.4.

$$\text{cavity growth rate} = \frac{\Delta V_{\text{cavity}}}{\Delta t_{\text{stage}}} \tag{3.4}$$

Figure 3.16 illustrates the results. Cavity growth appears to initially start with lower growth rates before reaching a peak rate as jetting progressed. The lower permeability cores that underwent jetting at 107 ft/s and 150 ft/s (dashed blue and orange lines) reached maximum cavity growth rate during the breakthrough stage, while the rest the cores peaked before breakthrough.

The average cavity growth rate for each rock sample can similarly be determined from the slopes of cavity growth linear regression analyses. Figures 3.17 to 3.19 show the linear regression, while Table 3.4 summarizes the results. All R^2 values are at least 0.95, except for one outlier with a 0.89 value. These indicate good linear regression fit.

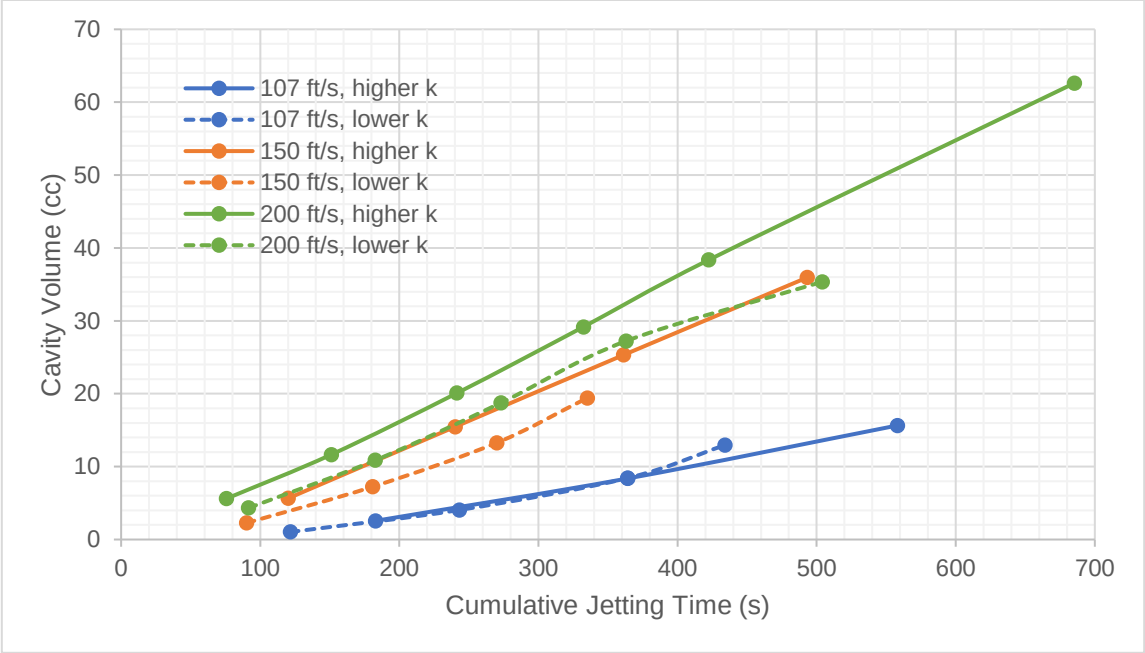

Figure 3.15. Cavity volume versus cumulative jetting time.

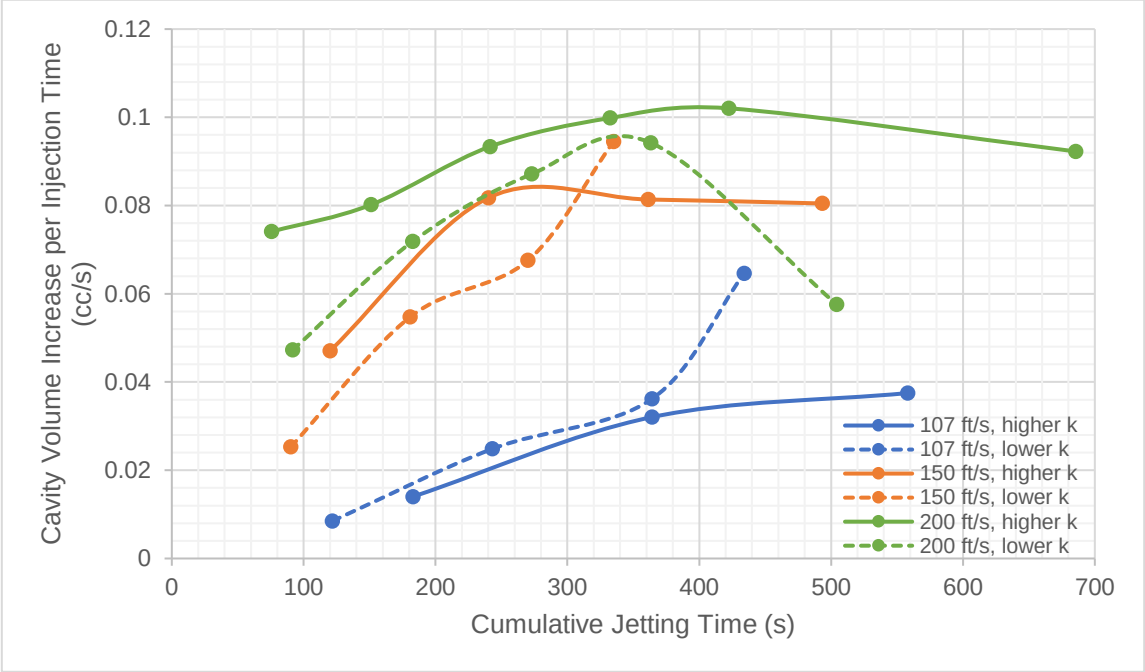

Figure 3.16. Cavity volume growth rate per stage versus cumulative jetting time.

Table 3.4. Average cavity growth rates for each rock sample, calculated through linear regression.

	Core ID	*k* (mD)	v_{jet} (ft/s)	ave cavity growth rate (cm^3/s)	R^2
1	IC01	4.01	107	0.0257	0.9501
2	IC02	2.43	107	0.0248	0.8881
3	IC03	6.87	150	0.0701	0.9866
4	IC05	2.38	150	0.0514	0.9413
5	IC04	5.30	200	0.0897	0.9967
6	IC06	3.53	200	0.0701	0.9876

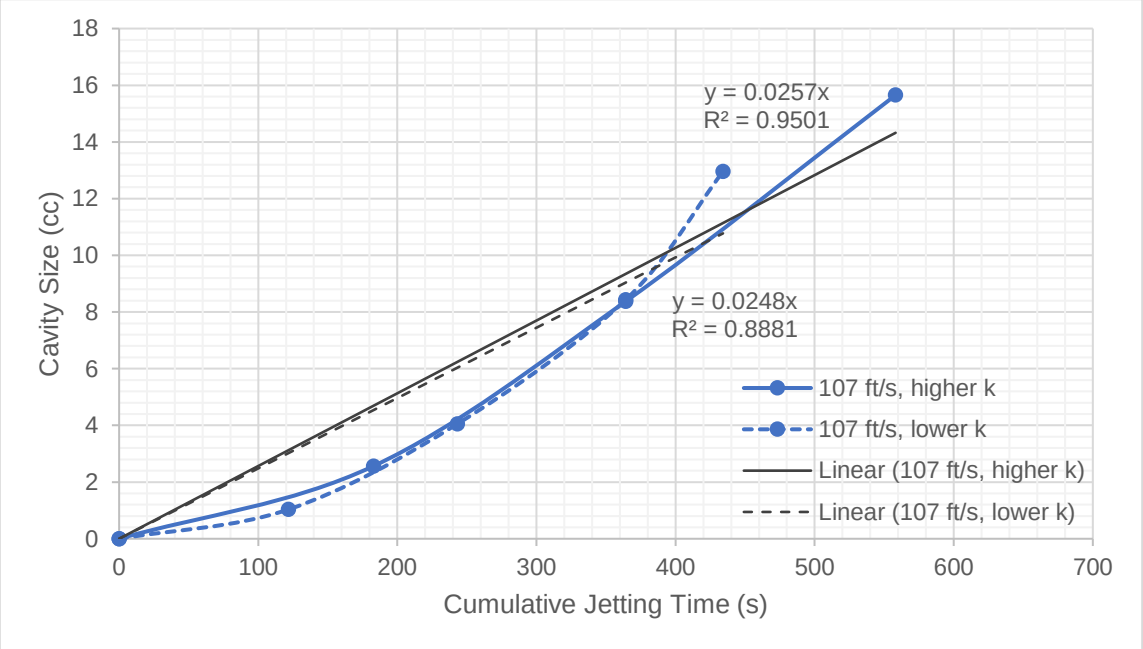

Figure 3.17. Average cavity growth rate calculation through linear regression (v_{jet} = 150 ft/s).

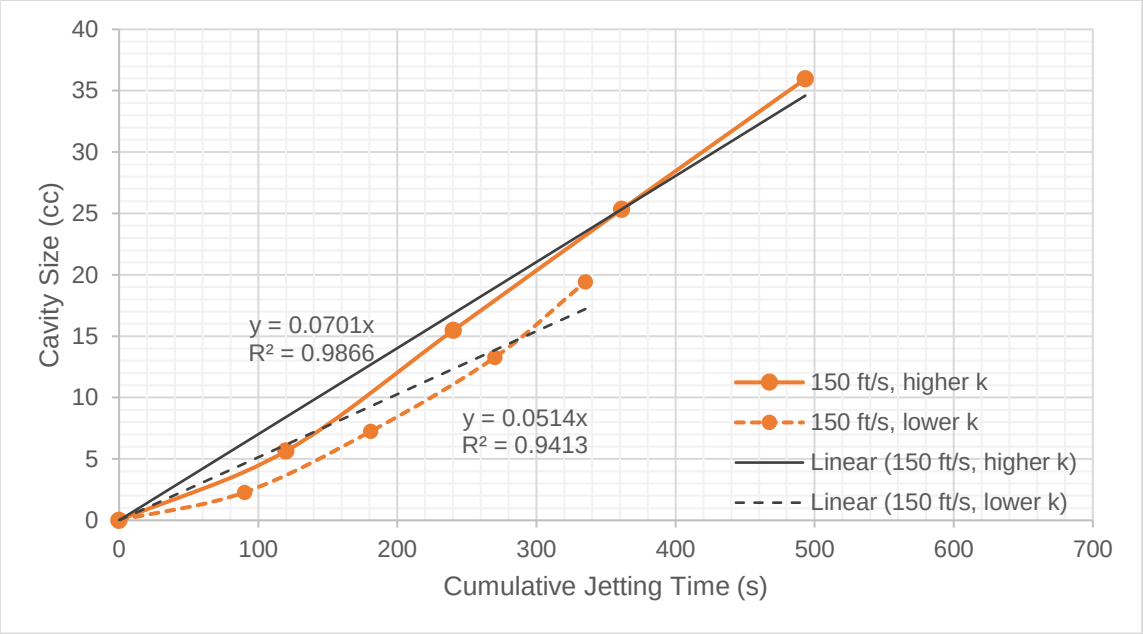

Figure 3.18. Average cavity growth rate calculation through linear regression (v_{jet} = 150 ft/s).

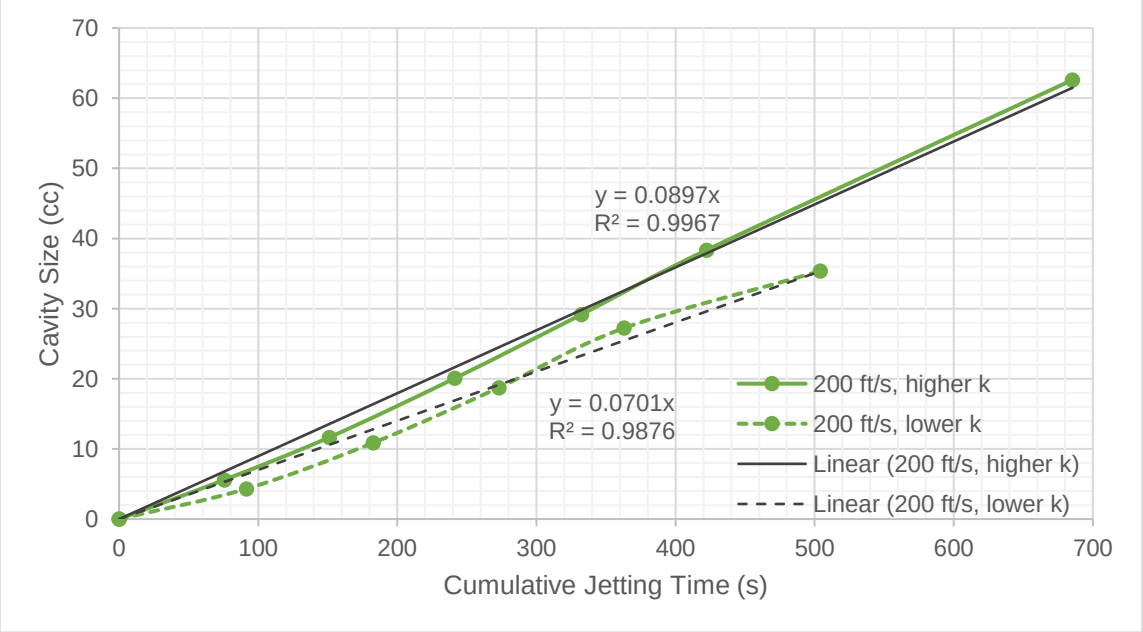

Figure 3.19. Average cavity growth rate calculation through linear regression (v_{jet} = 200 ft/s).

The linear regression analyses for average cavity growth rate calculation show that jetting at higher velocities cause faster average growth rates. Similarly, cores with higher permeabilities have higher average cavity growth rates than lower permeability cores.

Moreover, the linear regression analyses further support the observation that the cavity growth rates per stage increase as jetting progresses, and reaches a maximum during the later jetting stages. This is evidenced by the cavity volume curves starting out below their respective regression trend lines during the earlier stages, which then increase to above the trend line during the later jetting stages. This growth increase is more significant for cores that underwent jetting at lower jetting velocities (107 ft/s and 150 ft/s.)

4. CONCLUSIONS, RECOMMENDATIONS & FUTURE WORK

This study is successful in achieving its most essential goal – it revealed through multi-stage acid jetting experiments that cavities and wormholes grow concurrently. This finding serves as a fundamental knowledge in modeling the dissolution phenomenon of this acid stimulation technique. In addition, the study demonstrates a new methodology to process, visualize and generate 3D renderings of the cavities and wormholes by appropriating open source medical CT imaging software.

Wormhole analyses show that for cores that underwent the same jetting velocity, the ones with higher permeability take longer times to breakthrough, which is consistent with the matrix acidizing studies. Among these jetting velocities, 150 ft/s has the shortest breakthrough time followed by 107 ft/s, and 200 ft/s. However, no conclusive results can be drawn on the wormhole growth rates. This is due to imperfect experimental control on instantaneous interstitial velocity and the effects of residual acid concentration when switching from water jetting to acid jetting.

Cavity volume analyses show consistent, linear growth as jetting progressed. Cores with higher permeabilities form larger cavities, and similarly, those that underwent jetting at higher velocities form larger cavities. Cavity growth appears to start slowly during the initial stages, with peak growth rates at the middle to end stages.

The results of the study also expose the limitations of the current experimental set-up. Having variable instantaneous interstitial velocity hinders the potential to study the wormholing phenomenon during acid jetting in greater detail. It also limits the comparison

of results with matrix acidizing experiments. An ideal scenario is to set the interstitial velocity to be constant by automatically controlling the pressure differential across the core. Another approach is the addition of an effluent flow control device that chokes the outlet line proportionately in response to effluent weight increase, which directly translates to interstitial velocity.

The effects of residual acid concentration on multi-stage acid jetting can be minimized by treating the end of each stage as a breakthrough stage (i.e. shutting down the upstream backpressure) and at the same time adding flow control valves close to the injection line to divert further acid/water flow into the system. This method, however, keeps acid in the core matrix for an extended period of time and requires handling of live acid when removing the core from the holder.

Cavity growth can be studied on its own without wormholes by setting the interstitial velocity to zero (zero pressure differential across the core), as previous experiments have already explored (Holland, 2014). Studying the effects of jetting velocity, jetting time, and nozzle diameter on cavity behavior adds new knowledge to the understanding and modeling of acid jetting.

REFERENCES

Beckham, R.E., Shuchart, C. E., and Buechler, S. R. 2015. Impact of Acid Jetting on Carbonate Stimulation. Presented at the International Petroleum Technology Conference, Doha, Qatar, 6-9 December. IPTC 18360-MS.

Buijse, M.A. and Glasbergen, G. 2005. A Semiempirical Model to Calculate Wormhole Growth in Carbonate Acidizing. Presented at the SPE Annual Technical Conference and Exhibition, Dallas, Texas, 9-12 October. SPE 96892-MS.

Carpenter, C. 2013. Optimization of Limited-Entry Matrix Acid Stimulations in the Danish Central Graben. Journal of Petroleum Technology. Volume 65, Issue 06, June. SPE-0613–0096-JPT.

Denney, D. 2002. Single-Operation Stimulation of 14,000-Ft-Long Reservoir Sections. Journal of Petroleum Technology. Volume 54, Issue 11, November. SPE-1102–0044-JPT.

Dong, K., Jin, X., Zhu, D., and Hill, A.D. 2012. The Effect of Core Dimensions on the Optimum Acid Flux in Carbonate Acidizing. Presented at the SPE Formation Damage Conference, Lafayette, Louisiana, 26-28 February. SPE-168146-MS.

Etten, J., Zhu, D., and Hill, A. D. 2015. The Combined Effect of Permeability and Pore Structure on Carbonate Matrix Acidizing. Presented at EUROPEC 2015, Madrid, Spain, 1-4 June. SPE-174314-MS.

Grabski, E.R. 2012. Matrix Acidizing Core Flooding Apparatus: Equipment and Procedure Description. MS Thesis, Texas A&M University, College Station, Texas.

Hansen, J. H. and Nederveen, N. 2002. Controlled Acid Jet (CAJ) Technique for Effective Single Operation Stimulation of 14,000 ft Long Reservoir Sections. Presented at the European Petroleum Conference, Aberdeen, United Kingdom, 29–31 October. SPE-78318-MS.

Holland, C.C. 2014. Experimental High Velocity Acid Jetting in Limestone Carbonates. MS Thesis, Texas A&M University, College Station, Texas.

Johnson, A., Eslinger, D., and Larsen, H. 1998. An Abrasive Jetting Scale Removal System. Presented at the SPE/ICoTA Coiled Tubing Roundtable, Houston, Texas. 15–16 March. SPE-46026-MS.

Kalfayan, L. J., and Martin, A. N. 2009. The Art and Practice of Acid Placement and Diversion: History, Present State, and Future. Presented at the SPE Annual Technical Conference and Exhibition, New Orleans, Louisiana, 4-7 October. SPE-124141-MS.

Kocurek Industries. 2016. Indiana Limestone Carbonate Cores. 2016. http://www.kocurekindustries.com/indiana-limestone-3mD-cores (accessed 21 September 2016).

Ndonhong, V. 2014. Observations from Experimental Acid Jetting on Limestone Carbonates. MS Thesis, Texas A&M University, College Station, Texas.

Ndonhong, V., Belostrino, E., Zhu, D., Hill, A. D., Beckham, R. E., & Shuchart, C. E. 2016. The Impact of Rock Properties on Acid Jetting in Carbonate Rocks: An Experimental Study. Presented at the SPE Europec featured at 78th EAGE Conference and Exhibition, Vienna, Austria, 30 May-2 June. SPE 180113-MS.

Sau, R., Goodrow, A., Rockwell, M., Mayer, C., Shuchart, C. E., and Grubert, M. A. 2014. An Integrated Software Technology Based on Research and Field Application for Completion, Stimulation and Fluid Placement Design in Complex Wells. Presented at the International Petroleum Technology Conference, Kuala Lumpur, Malaysia. 10-12 December. IPTC-17870-MS.

Sau, R., Shuchart, C. E., and Grubert, M. 2014. Advanced Completion and Stimulation Design Model for Maximum Reservoir Contact Wells. Presented at the Abu Dhabi International Petroleum Exhibition and Conference, Abu Dhabi, UAE, 10-13 November. SPE-171800-MS.

Seletchi, E. and Duliu, O.G., 2007. Image Processing and Data Analysis in Computed Tomography. Romanian Journal of Physics, pp. 764-774. Volume 72. Bucharest, Romania. January.

Shuchart, C. E. 2014. Completion and Stimulation of Maximum Reservoir Contact and Complex Wells. Presentation at the SPE Stimulation Applied Technology Workshop, Abu Dhabi, UAE, 24-25 February.

Surjaatmadja, J., Abass, H., and Brumley, J. 1994. Elimination of Near-Wellbore Tortuosities by Means of Hydrajetting. Presented at the Asia Pacific Oil and Gas Conference, Melbourne, Australia, 7-10 November. SPE 28761-MS.

APPENDIX

Figure A.1. Post-jetting core images showing cavities (top view).

Figure A.2. Post-jetting core images showing wormholes (bottom view).

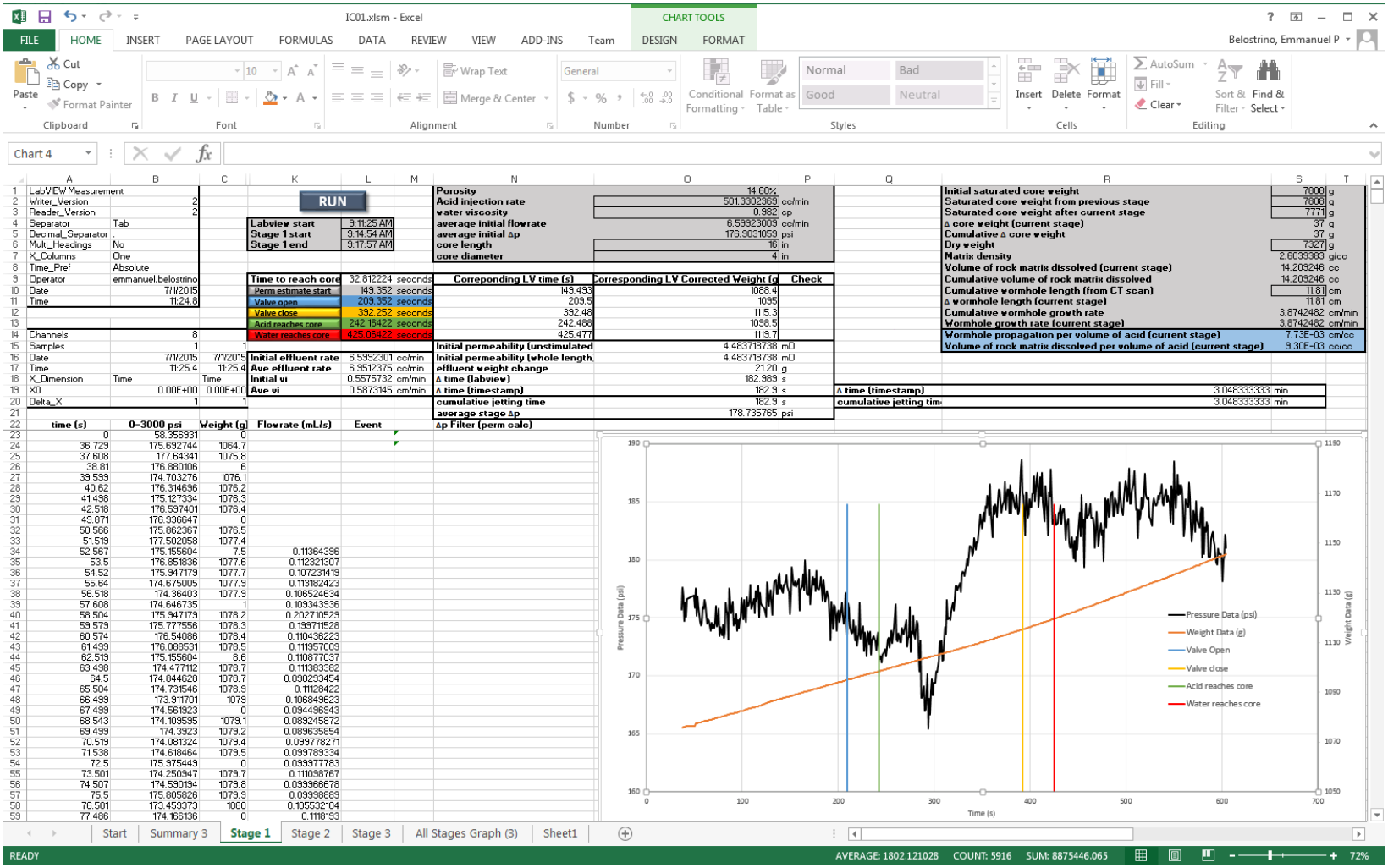

Figure A.3. Excel file for results processing.

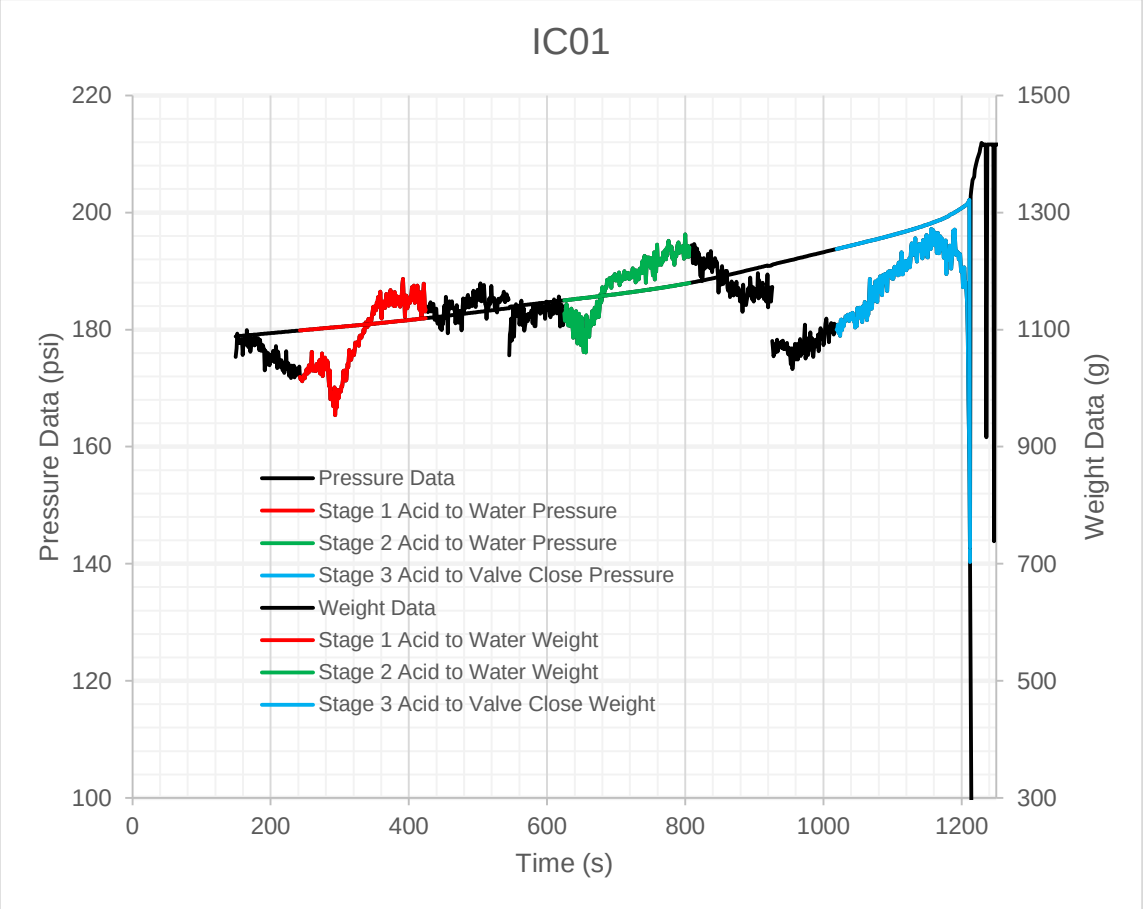

Figure A.4. IC01 (v_{jet} = 107 ft/s, k = 4.01 mD) multi-stage acid jetting results.

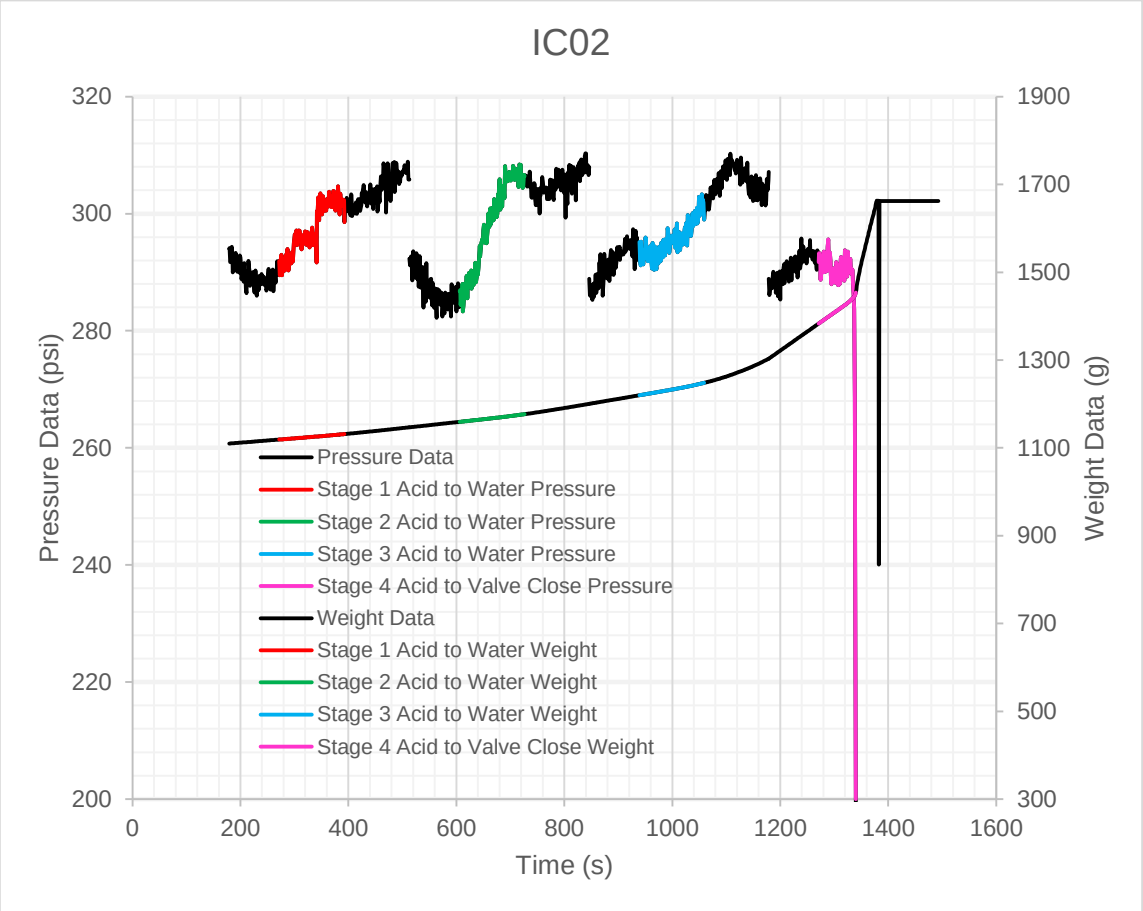

Figure A.5. IC02 (v_{jet} = 107 ft/s, k = 2.43 mD) acid jetting results.

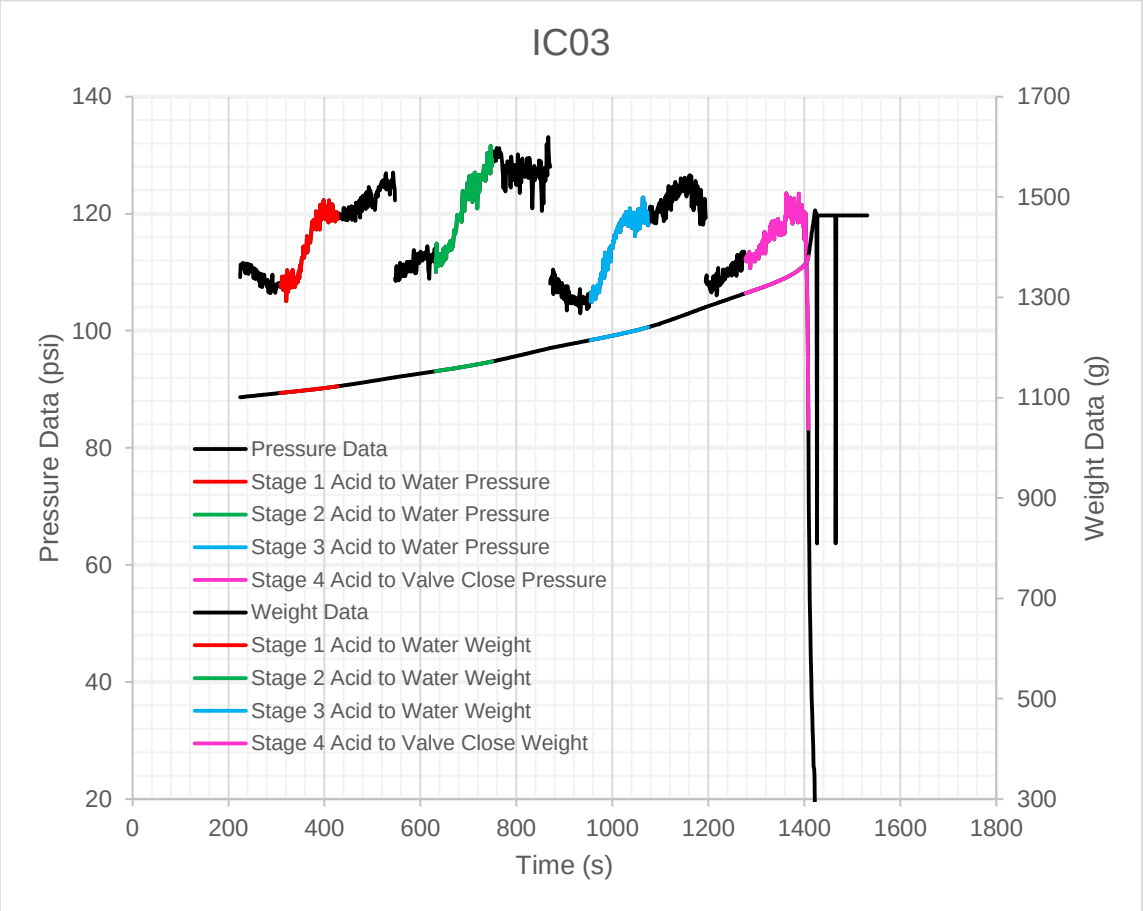

Figure A.6. IC03 (v_{jet} = 150 ft/s, k = 6.87 mD) acid jetting results.

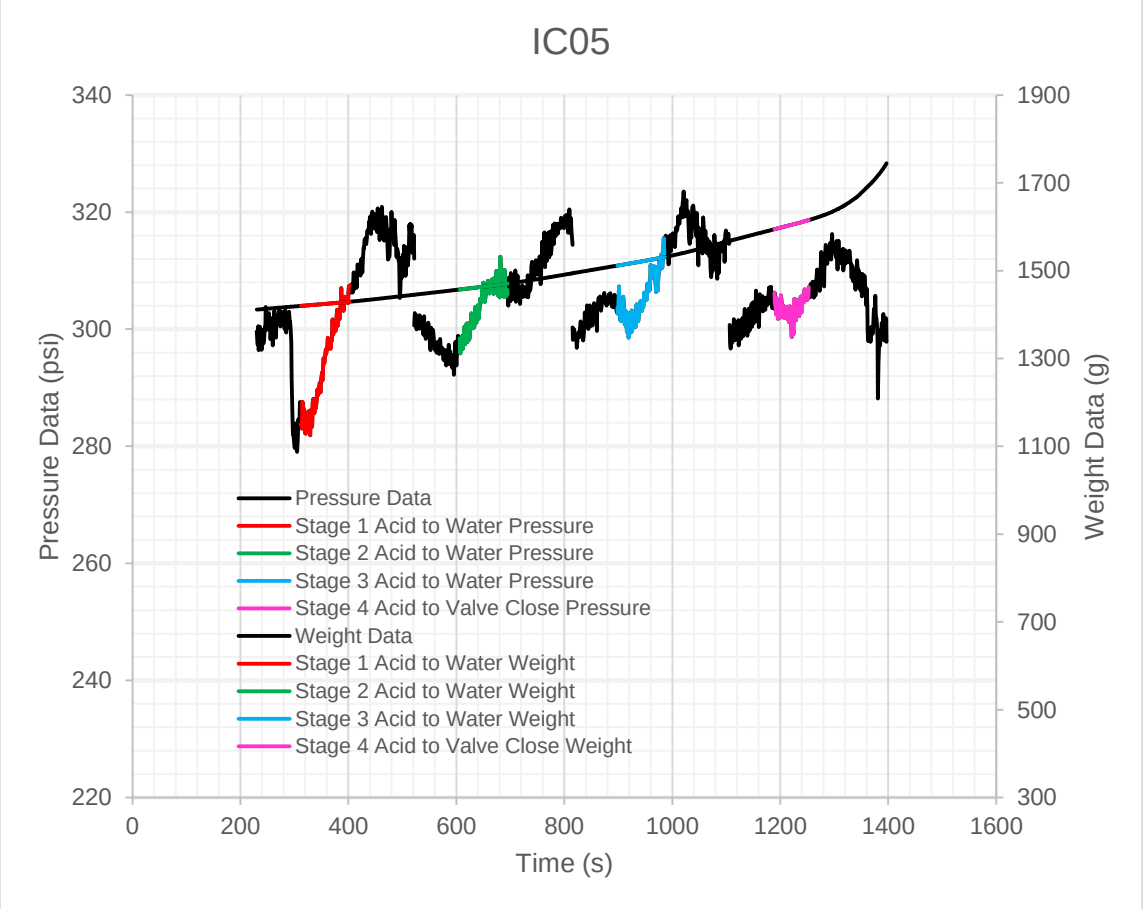

Figure A.7. IC05 (v_{jet} = 150 ft/s, k = 2.38 mD) acid jetting results.

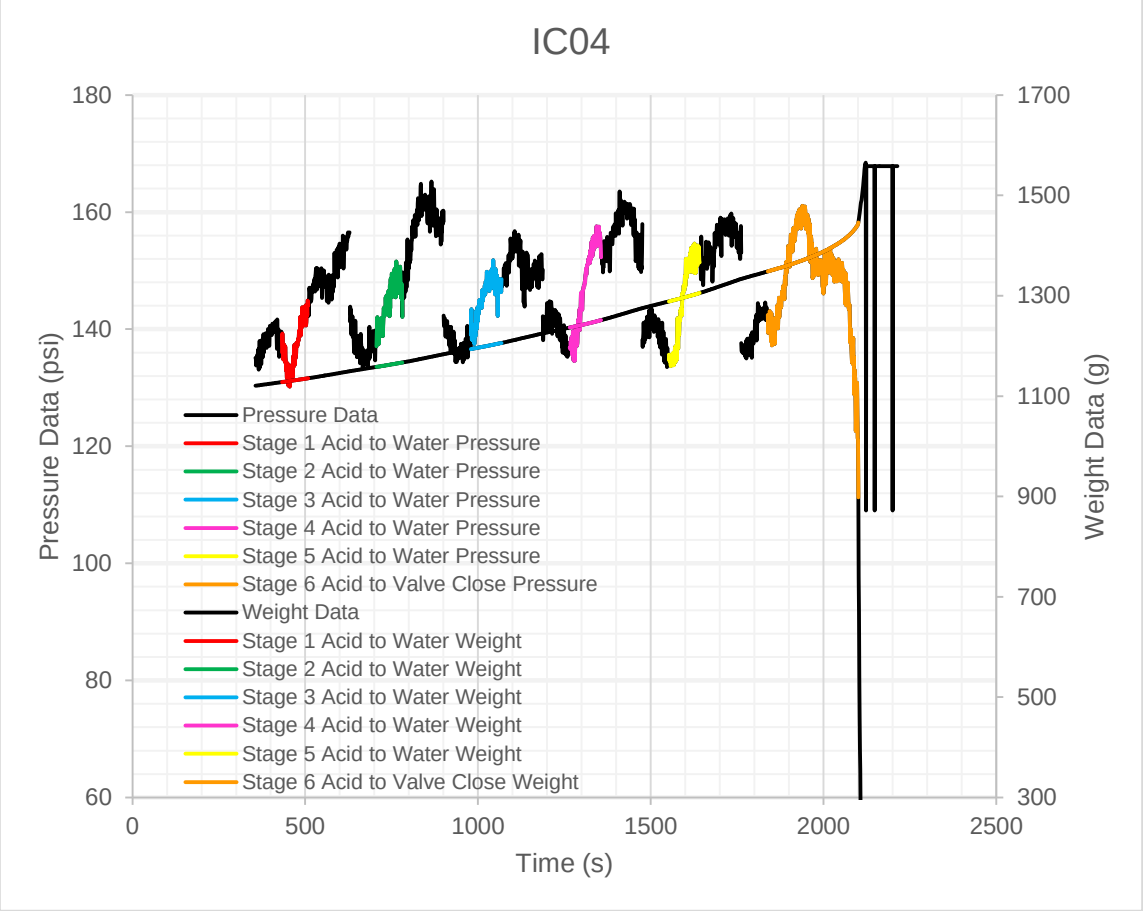

Figure A.8. IC04 (v_{jet} = 200 ft/s, k = 5.30 mD) acid jetting results.

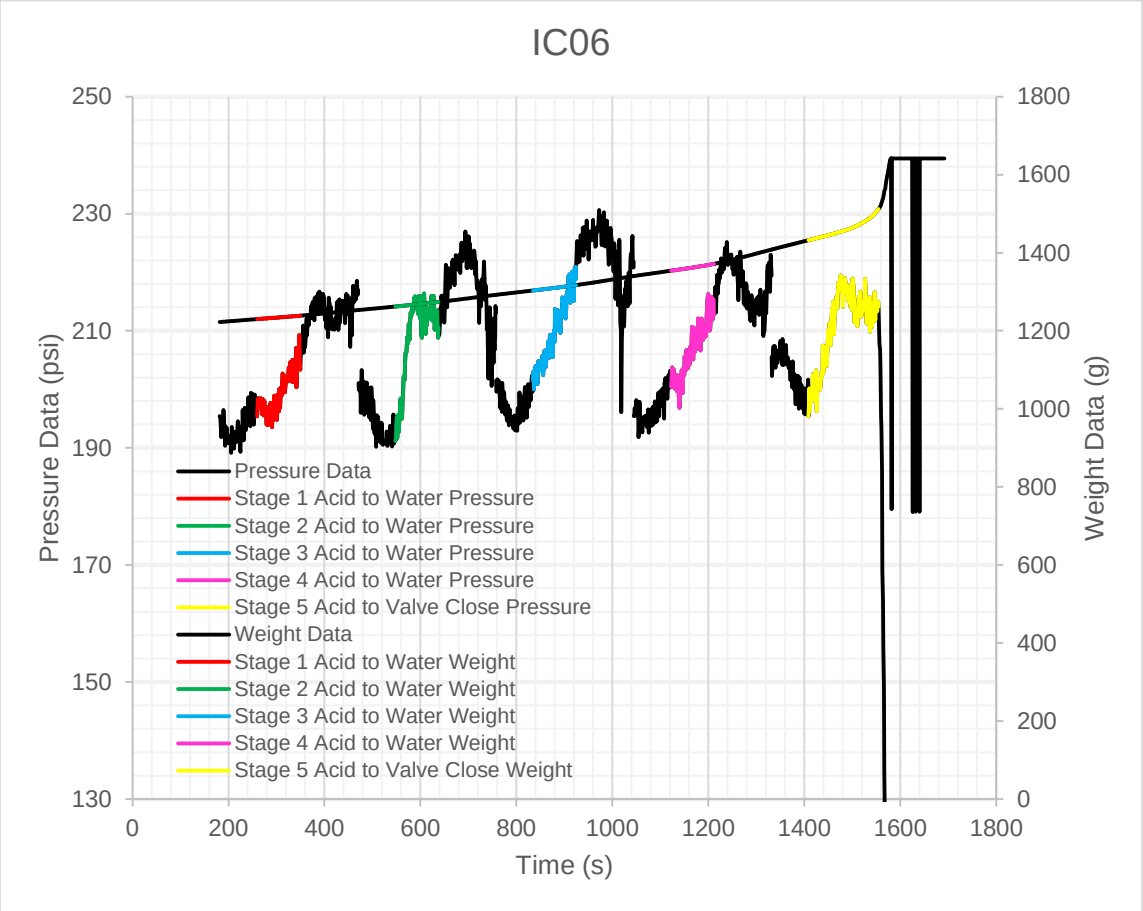

Figure A.9. IC06 (v_{jet} = 200 ft/s, k = 3.53 mD) acid jetting results.

Table A.1. IC01 (v_{jet} = 107 ft/s, k = 4.01 mD) CT image processing results.

Stage	Inj Time (s)	Cum Jetting Time (s)	Cavity Volume (cc)	Δ Cavity Vol (cc)	Cavity Growth per Inj Time (cc/s)	Cumulative Wormhole Length (cm)	Δ Wormhole Length per Stage (cm)	Δ Wormhole Length per Inj Time (cm/s)	Ave vi (cm/s)
1	182.9	182.9	2.56	2.56	0.014	11.81	11.81	0.065	0.59
2	181.3	364.2	8.38	5.81	0.032	27.87	16.06	0.089	0.83
3	194.0	558.2	15.65	7.27	0.038	40.62	12.75	0.066	2.37

Table A.2. IC02 (v_{jet} = 107 ft/s, k = 2.43 mD) CT image processing results.

Stage	Inj Time (s)	Cum Jetting Time (s)	Cavity Volume (cc)	Δ Cavity Vol (cc)	Cavity Growth per Inj Time (cc/s)	Cumulative Wormhole Length (cm)	Δ Wormhole Length per Stage (cm)	Δ Wormhole Length per Inj Time (cm/s)	Ave vi (cm/s)
1	121.8	121.8	1.03	1.03	0.008	10.72	10.72	0.088	0.53
2	121.4	243.2	4.05	3.02	0.025	21.95	11.23	0.093	0.75
3	120.9	364.1	8.43	4.37	0.036	37.22	15.27	0.126	1.22
4	70.0	434.1	12.95	4.53	0.065	40.62	3.4	0.049	5.72

Table A.3. IC03 (v_{jet} = 150 ft/s, k = 6.87 mD) CT image processing results.

Stage	Inj Time (s)	Cumulative Jetting Time (s)	Cavity Volume (cc)	Δ Cavity Vol (cc)	Cavity Growth per Inj Time (cc/s)	Cumulative Wormhole Length (cm)	Δ Wormhole Length per Stage (cm)	Δ Wormhole Length per Inj Time (cm/s)	Ave vi (cm/s)
1	120	120	5.65	5.65	0.047	11.64	11.64	0.097	0.55
2	120.2	240.2	15.47	9.83	0.082	21.74	10.1	0.084	0.80
3	121.1	361.3	25.33	9.85	0.081	30.6	8.86	0.073	1.05
4	132.0	493.3	35.95	10.62	0.080	40.61	10.01	0.076	2.94

Table A.4. IC05 (v_{jet} = 150 ft/s, k = 2.38 mD) CT image processing results.

Stage	Inj Time (s)	Cumulative Jetting Time (s)	Cavity Volume (cc)	Δ Cavity Vol (cc)	Cavity Growth per Inj Time (cc/s)	Cumulative Wormhole Length (cm)	Δ Wormhole Length per Stage (cm)	Δ Wormhole Length per Inj Time (cm/s)	Ave vi (cm/s)
1	90.2	90.2	2.28	2.28	0.025	10.73	10.73	0.119	0.54
2	90.6	180.8	7.24	4.96	0.055	20.24	9.51	0.105	0.77
3	89.3	270.1	13.28	6.04	0.068	28.3	8.06	0.090	1.14
4	65.00	335.1	19.42	6.15	0.095	40.63	12.33	0.190	1.69

Table A.5. IC04 (v_{jet} = 200 ft/s, k = 5.30 mD) CT image processing results.

Stage	Inj Time (s)	Cumulative Jetting Time (s)	Cavity Volume (cc)	Δ Cavity Vol (cc)	Cavity Growth per Inj Time (cc/s)	Cumulative Wormhole Length (cm)	Δ Wormhole Length per Stage (cm)	Δ Wormhole Length per Inj Time (cm/s)	Ave vi (cm/s)
1	75.6	75.6	5.60	5.60	0.074	5.98	5.98	0.079	0.51
2	75.5	151.1	11.66	6.05	0.080	10.46	4.48	0.059	0.59
3	90.3	241.4	20.09	8.43	0.093	15.08	4.62	0.051	0.70
4	91	332.4	29.17	9.09	0.100	20.2	5.12	0.056	0.82
5	90	422.4	38.36	9.18	0.102	24.33	4.13	0.046	0.95
6	263.0	685.4	62.62	24.27	0.092	40.64	16.31	0.062	1.96

Table A.6. IC06 (v_{jet} = 200 ft/s, k = 3.53 mD) CT image processing results.

Stage	Inj Time (s)	Cumulative Jetting Time (s)	Cavity Volume (cc)	Δ Cavity Vol (cc)	Cavity Growth per Inj Time (cc/s)	Cumulative Wormhole Length (cm)	Δ Wormhole Length per Stage (cm)	Δ Wormhole Length per Inj Time (cm/s)	Ave vi (cm/s)
1	91.6	91.6	4.33	4.33	0.047	8.33	8.33	0.091	0.51
2	91	182.6	10.87	6.54	0.072	15.97	7.64	0.084	0.68
3	90.4	273	18.75	7.88	0.087	22.57	6.6	0.073	0.81
4	90.1	363.1	27.24	8.49	0.094	30.42	7.85	0.087	1.03
5	141.005	504.1	35.36	8.12	0.058	40.62	10.2	0.072	2.90